

EFFECTS OF PRESSURE DISTRIBUTION ON THE SHAPE OF  
TENSION SHELL ENTRY VEHICLES

By

James Wayne Sawyer

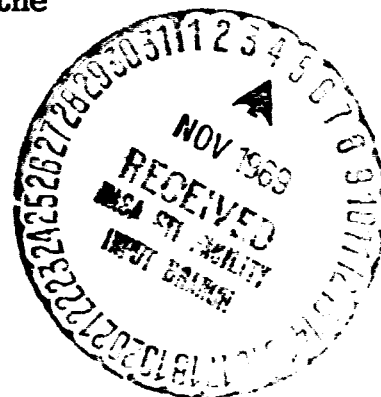
Thesis submitted to the Graduate Faculty of the  
Virginia Polytechnic Institute

in partial fulfillment for the degree of

MASTER OF SCIENCE

in

Engineering Mechanics



April 1969

FACILITY FORM 602	<b>N69-40219</b>	(ACCESSION NUMBER)
	<b>62</b>	(PAGES)
	<b>TMX-61917</b>	(NASA CR OR TMX OR AD NUMBER)
	<b>32</b>	(CATEGORY)

EFFECTS OF PRESSURE DISTRIBUTION ON THE SHAPE OF  
TENSION SHELL ENTRY VEHICLES

By

James Wayne Sawyer

ABSTRACT

Theoretical and experimental investigations were conducted for the purpose of improving accuracy in calculating pressure distributions for various tension shell decelerator shapes and evaluating the effects on derived shapes resulting from the application of different pressure distributions. Although tension shell shapes have been derived using Newtonian aerodynamics in conjunction with linear membrane theory, experimental pressure distributions obtained on other bluff shapes indicated that Newtonian theory does not describe the actual pressure distribution. However, better agreement has been obtained for many bluff shapes with sonic corners by means of integral relation theory. Consequently, a computational procedure involving the use of a one-strip integral relation technique for calculating pressure distributions was devised for use in deriving new tension shell shapes. Inasmuch as the nose radius and the free-stream Mach number affected the integral relation pressure distributions, their effects on integral-relation-derived tension shell shapes were investigated.

Experimental pressure distributions were obtained at a Mach number of 3.0 in the Langley 9- by 6-foot thermal structures tunnel and are presented for typical Newtonian- and integral-relation-derived tension

shell shapes. The experimental pressures are presented in tabular and graphical form and are compared with pressures obtained from the Newtonian and integral relation theories. Tension shell shapes were then derived using the experimental pressure distributions in conjunction with linear membrane theory and were compared with the Newtonian- and integral-relation-derived tension shell shapes.

EFFECTS OF PRESSURE DISTRIBUTION ON THE SHAPE OF  
TENSION SHELL ENTRY VEHICLES

by

James Wayne Sawyer

Thesis submitted to the Graduate Faculty of the  
Virginia Polytechnic Institute  
in partial fulfillment for the degree of

MASTER OF SCIENCE

in

Engineering Mechanics

APPROVED:

\_\_\_\_\_  
Dr. R. T. Davis, Chairman

\_\_\_\_\_  
  
\_\_\_\_\_  
  
\_\_\_\_\_

April 1969

Blacksburg, Virginia

## II. TABLE OF CONTENTS

CHAPTER		PAGE
I.	TITLE . . . . .	i
II.	TABLE OF CONTENTS . . . . .	ii
III.	ACKNOWLEDGMENTS . . . . .	iv
IV.	LIST OF TABLES AND FIGURES . . . . .	v
V.	LIST OF SYMBOLS . . . . .	vii
VI.	INTRODUCTION . . . . .	1
VII.	ANALYSIS . . . . .	4
	A. Statement of Problem . . . . .	4
	B. Basic Equations and Solutions . . . . .	4
	1. Structural . . . . .	4
	2. Aerodynamic . . . . .	7
	C. Calculation Procedure . . . . .	9
VIII.	EXPERIMENT . . . . .	11
	A. Models . . . . .	11
	B. Test Apparatus . . . . .	11
	1. Test Facility . . . . .	11
	2. Instrumentation . . . . .	12
	C. Test Procedure . . . . .	12
IX.	THEORETICAL RESULTS AND DISCUSSION . . . . .	13
	A. Comparison of Newtonian and Integral Relation	
	Pressure Distributions and Corresponding	
	Tension Shell Shapes . . . . .	13

CHAPTER	PAGE
B. Effects of Nose Radius and Mach Number on Shapes and Pressure Distributions Derived From Integral Relation Theory . . . . .	15
X. EXPERIMENTAL RESULTS AND DISCUSSION . . . . .	17
XI. COMPARISON OF THEORY AND EXPERIMENT . . . . .	18
A. Pressure Distribution . . . . .	18
B. Shapes Determined From Experimental Pressures . . .	18
C. Drag Coefficients . . . . .	19
XII. CONCLUDING REMARKS . . . . .	21
XIII. REFERENCES . . . . .	23
XIV. VITA . . . . .	25
XV. APPENDIX A . . . . .	26

### III. ACKNOWLEDGMENTS

The author wishes to express his appreciation to the National Aeronautics and Space Administration for permission to conduct the research for this thesis during duty hours. He also wishes to thank Dr. R. T. Davis of the Engineering Mechanics Department of Virginia Polytechnic Institute for his assistance and encouragement in the development of this thesis.

#### IV. LIST OF TABLES AND FIGURES

TABLE	PAGE
I. Coordinates and Orifice Locations for Newtonian- and Integral-Relation-Derived Pressure Distribution Models . . . . .	30
II. Coordinates for Newtonian- and Integral-Relation- Derived Tension Shell Shapes . . . . .	31
III. Integral Relation Pressure Distributions and Drag Coefficients for Tension Shell Shapes . . . . .	32
IV. Experimental Pressure Data for $Z = 0.65$ Tension Shell Shapes With $r_n/r_b = 0.20$ . . . . .	33
V. Experimental Pressure Distributions and the Derived $Z = 0.65$ Tension Shell Shapes . . . . .	34
VI. Theoretical and Experimental Drag Coefficients for the $Z = 0.65$ Newtonian- and Integral-Relation- Derived Tension Shell Shapes With $r_n/r_b = 0.20$ . . .	35
FIGURE	
1. Typical tension shell entry vehicle . . . . .	36
2. Tension shell shape and coordinate system . . . . .	37
3. Geometry and coordinate system for aerodynamic consideration . . . . .	38
4. Pressure distribution model details . . . . .	39
5. Photograph of tension shell models . . . . .	40
6. Illustration of model sting mount system . . . . .	41



FIGURE	PAGE
7. Theoretical pressure distributions for the $Z = 0.65$ Newtonian-derived tension shell shape with $r_n/r_b = 0.05$ . . . . .	42
8. Comparison of Newtonian and integral relation pressure distributions and corresponding tension shell shapes . . . . .	43
9. Effects of nose radius on the integral relation pressure distributions and derived tension shell shapes at $M_\infty = 3.0$ . . . . .	46
10. Effects of Mach number on the integral relation pressure distributions and derived tension shell shapes with $r_n/r_b = 0.05$ . . . . .	47
11. Experimental and theoretical pressure distributions about the $Z = 0.65$ Newtonian- and integral-relation- derived tension shell shapes with $r_n/r_b = 0.20$ and at $M_\infty = 3.0$ . . . . .	48
12. Comparison of the $Z = 0.65$ Newtonian-, integral- relation-, and experimentally derived tension shell shapes and pressure distributions . . . . .	50

## V. LIST OF SYMBOLS

A	projected area
$A_b$	projected base area, $\pi r_b^2$
a	sonic velocity
C	constant used in Newtonian pressure distribution
$C_D$	drag coefficient, $\frac{\int C_p dA}{A_b}$
$C_p$	pressure coefficient, $p - p_\infty$
$C_{p,stag}$	stagnation pressure coefficient behind normal shock
d	maximum model diameter
K	body surface curvature, nondimensionalized by $r_b$
$M_\infty$	free-stream Mach number
$N_0$	$N_\varphi$ evaluated at $r = r_b$
$N_\alpha, N_\varphi$	circumferential and meridional stress resultants, respectively, positive in tension
P	nondimensional membrane pressure differential, $p - p_b$
p	local surface pressure, nondimensionalized by $q_\infty$
$p_b$	base pressure, nondimensionalized by $q_\infty$
$q_\infty$	free-stream dynamic pressure
R	nondimensional model coordinates, $\frac{r}{r_b}$
$r_b$	base radius

$r_n$	model nose radius (see fig. 3)
$r_m, r_c$	principal radii of curvature of shell in meridional and circumferential directions, respectively
$s^*$	sonic point on model surface
$s, n$	curvilinear coordinates along, and normal to, body surface nondimensionalized by $r_b$ (see fig. 3)
$u, v$	velocity components in $s$ - and $n$ -direction, respectively, nondimensionalized by free-stream velocity
$X$	nondimensional model coordinate, $\frac{x}{r_b}$
$x, r$	model coordinates (see fig. 2)
$Z = \frac{q_\infty r_b}{N_0}$	tension shell shape parameter
$\alpha = \frac{N_\alpha}{N_\varphi}$	
$\beta$	shock angle (see fig. 3)
$\xi$	shock-layer thickness along $n$ -coordinate nondimensional- ized by $r_b$ (see fig. 3)
$\gamma$	ratio of specific heats
$\lambda = \beta - \theta$	
$\theta = \frac{\pi}{2} - \varphi$	surface slope
$\Phi$	stagnation streamline isentropic constant, $\frac{P_1(0)}{(\rho_1(0))^\gamma}$
$\rho$	density, nondimensionalized by $\rho_\infty$

$\tau$	combined entropy-continuity flow variable, $\left(\frac{p}{\rho\Phi}\right)^{1/\gamma-1}$
$\psi, \varphi$	circumferential and meridional coordinates, respectively
Subscripts	
0	quantities along surface ( $n = 0$ )
1	quantities along shock wave ( $n = \delta$ )
$\infty$	free-stream conditions

## VI. INTRODUCTION

The possibility of exploring the atmospheres of certain planets has stimulated the development of aerodynamic decelerators (refs. 1 through 15). The entry of unmanned probes into an atmosphere requires a vehicle with low structural weight that can generate a high drag coefficient in order to obtain a reasonable dwell time in the atmosphere for the gathering and transmission of data. One type of decelerator that shows promise of satisfying the above requirements is the tension shell as derived in reference 1. A typical tension shell configuration is shown in figure 1. The payload is assumed to be concentrated in the forward portion of the vehicle which is connected to the compression ring at the rear by a thin shell or membrane whose shape is characterized by negative Gaussian curvature. The configurations obtain their name from the fact that the shell is shaped so as to resist the aerodynamic loading by means of tensile stresses only.

As indicated by the references 2 through 10, the tension shell concept has been extensively studied aerodynamically over a wide range of Mach number, Reynolds number, and fineness ratios. The results from the investigation of reference 2 indicate that the relatively bluff tension shell shapes - that is, those that generate a detached bow shock wave - may be best suited for use as entry vehicles because they can develop relatively high drag coefficients without the adverse boundary-layer flow separation effects that are encountered by less bluff tension shell shapes. In previous investigations of this concept, the tension shell shapes were derived using linear membrane theory in conjunction with

either an axisymmetric Newtonian or a constant pressure distribution. However, the experimental data of reference 16 for large angle cones indicated that the constant pressure distribution predicted by Newtonian theory does not describe the actual distribution to which the cones are subjected. Thus, this inadequacy of the Newtonian theory with respect to cones having proportions similar to those of the bluff tension shell shapes poses the question of how the shapes of reference 1 might differ from shapes that are derived using a more realistic pressure distribution. Moreover, the question arises concerning the nature of the actual pressure distribution on bluff tension shell shapes inasmuch as no experimental pressures are presently available.

In view of the above questions, an investigation was made to determine a more realistic pressure distribution and its effect on the bluff tension shell shapes of reference 1. One theoretical approach that accurately predicts the pressure distribution of large-angle cones is the integral relation theory explained in reference 16. Consequently, a computational procedure was devised in the present investigation involving the use of a one-strip integral relation technique for calculating pressure distributions and linear membrane theory to derive new tension shell shapes. Shapes were also derived using pressures obtained from wind-tunnel tests conducted at Mach 3.0 on models with shapes that were derived from Newtonian pressures and from pressures predicted by the integral relation method.

The present thesis presents the analysis for shape determination, discusses the results from the theoretical study and from experiment,

and compares the shapes obtained from the different pressure distributions. Inasmuch as the pressure distributions given by the integral relation method are somewhat dependent on Mach number and nose radius, the effects of varying the Mach number from 2.5 to 7.0 and of varying the nose radius from 0.05 to 0.56 times the base radius on the derived shapes are also discussed.

## VII. ANALYSIS

### A. Statement of Problem

The following analysis consists of solving two sets of independent differential equations with their respective boundary conditions. The first set of equations comes from the linear membrane equilibrium equations for a shell of revolution subjected to an axisymmetric pressure distribution. Circumferential and meridional stress resultants are assumed related to each other by a constant, and zero axial forces are assumed on the compression ring. The second set of equations is derived by applying integral relation theory to the solution of supersonic, inviscid flow around bluff bodies. The body surface is assumed to be normal to the free-stream flow direction at the nose, and the local velocity is assumed to be sonic at the sharp corner on the base compression ring. The two sets of equations are related in that the first set of equations requires a pressure distribution as an input in order to provide a shape, while the second set of equations requires a shape as an input in order to provide a pressure distribution. Either a particular shape or a pressure distribution must be assumed to start the calculations, and an iterative procedure must be followed between the two sets of equations until a unique shape and pressure distribution are obtained.

### B. Basic Equations and Solutions

1. Structural. - For a shell of revolution subject to an axisymmetric pressure distribution, the appropriate linear membrane equilibrium



equations are (see ref. 1):

$$\frac{d(rN_\varphi)}{d\varphi} - r_m N_\alpha \cos \varphi = 0 \quad (1)$$

and

$$\frac{N_\varphi}{r_m} + \frac{N_\alpha}{r_c} = p q_\infty \quad (2)$$

where (see fig. 2)

$$\frac{1}{r_m} = \cos \varphi \frac{d\varphi}{dr} = \frac{d(\sin \varphi)}{dr} \quad (3)$$

and

$$\frac{1}{r_c} = \frac{\sin \varphi}{r} \quad (4)$$

Assuming  $N_\alpha = \alpha N_\varphi$ , where  $\alpha$  is a constant, equation (1) becomes

$$\frac{dN_\varphi}{dr} + \frac{1 - \alpha}{r} (N_\varphi) = 0 \quad (5)$$

Solving for  $N_\varphi$ :

$$r^{(1-\alpha)} N_\varphi = \text{constant} = N_0 r_b^{(1-\alpha)} \quad (6)$$

Let  $Z$  (which corresponds to the value of  $A^2$  used in ref.1) be given as follows:

$$Z = \frac{q_\infty r_b}{N_0} \quad (7)$$

With the use of equations (3), (4), (6), and (7), equation (2) becomes

$$\frac{d\varphi}{dr} + \frac{\alpha \sin \varphi}{r \cos \varphi} - \frac{ZP}{r_b \cos \varphi} \left( \frac{r}{r_b} \right)^{(1-\alpha)} = 0 \quad (8)$$

If  $R = \frac{r}{r_b}$ , then  $dR = \frac{dr}{r_b}$  and equation (8) becomes

$$\frac{d\varphi}{dR} + \frac{\alpha \sin \varphi}{R \cos \varphi} - \frac{Zp}{\cos \varphi} (R)^{(1-\alpha)} = 0 \quad (9)$$

Assuming that there is no axial force on the compression ring, the slope of the model surface becomes zero at  $r = r_t$ , or

$$\frac{dx}{dr} = -\tan \varphi = 0 \quad (10)$$

Thus, for any particular pressure distribution, there exists a first-order differential equation and the necessary boundary conditions to solve for the model surface slope. Equation (9) may again be integrated with respect to  $r$  to obtain the  $x$ -coordinate of the desired configuration as a function of  $r$ .

Equation (9), subject to the boundary condition (eq. (10)), has been solved for a body of revolution with an axisymmetric pressure distribution by the use of a digital computer. A source program in Fortran IV language is given in appendix A. Equation (9) was numerically integrated twice using the fourth-order Runge-Kutta integration technique. The integration was started at  $R = 1$  and continued with decreasing values to  $R = 0$ . In order to use the program, values of  $Z$ ,  $\alpha$ ,

integration step height,  $DR$ , and a pressure distribution as a function of  $R$  are necessary inputs to the program. The program output consists of values of the axial coordinate and surface slope as a function of  $R$ . With this program, shapes are obtained with zero nose radius of curvature.

2. Aerodynamic. - For a blunt body of revolution with sharp corners subjected to inviscid supersonic flow, the governing differential equations for the one-strip method may be written as follows (see ref. 16):

$$\frac{d\delta}{ds} = (1 + K\delta)\tan \lambda \quad (11)$$

$$\begin{aligned} \frac{d\beta}{ds} = & \left[ (1 + K\delta) \left( \tan \lambda - \frac{\delta \sin \theta}{r_0} \right) \rho_1 u_1 v_1 - (2 + K\delta) \frac{r_1}{r_0} \rho_1 v_1^2 + K\delta \rho_0 u_0^2 \right. \\ & \left. + \left( 1 + K\delta + \frac{r_1}{r_0} \right) (p_0 - p_1) \right] \left( \delta \frac{r_1}{r_0} \frac{\partial \rho_1 u_1 v_1}{\partial \beta} \right)^{-1} \end{aligned} \quad (12)$$

and

$$\begin{aligned} \frac{du_0}{ds} = & \left\{ (\tau_1 u_1 - \tau_0 u_0) \frac{d\delta}{ds} - \frac{\delta \sin \theta}{r_0} [\tau_0 u_0 + (1 + K\delta) \tau_1 u_1] \right. \\ & \left. - \frac{r_1}{r_0} \left[ \delta \frac{\partial}{\partial \beta} (\tau_1 u_1) \frac{d\beta}{ds} + (2 + K\delta) \tau_1 v_1 \right] \right\} \left[ \delta \tau_0 (1 - M_0^2) \right]^{-1} \end{aligned} \quad (13)$$

A sketch of the geometry and coordinates are shown in figure 3. A particular body contour is specified by giving the surface angle and curvature as a function of  $s$ . On the axis of symmetry at  $s = 0$ , the

body surface must be normal to the stream direction  $\theta(0) = \frac{\pi}{2}$  and the surface slope must be continuous; thus, the following conditions hold:

$$\beta(0) = \frac{\pi}{2} \quad (14)$$

and

$$u(0) = 0 \quad (15)$$

The surface speed is required to reach sonic velocity at the model corner,  $r = r_b$ , which results in the boundary condition that

$$u_0(s^*) = a^* \quad (16)$$

where  $a^*$  is a constant dependent on  $M_\infty$  and  $\gamma$ . Thus, we have three interconnected first-order differential equations (11), (12), and (13), and three boundary conditions, (14), (15), and (16), that must be satisfied. The functions at the shock wave are explicit functions of  $\gamma$ ,  $M_\infty$ ,  $\beta$ , and  $\theta$ . The main dependent variables are  $\delta$ ,  $\beta$ , and  $u_0$ , while  $p_0$  and  $\rho_0$  are obtained as explicit functions of  $\gamma$ ,  $M_\infty$ , and  $u_0$  by using the isentropic law.

Equations (11), (12), and (13) and the boundary conditions (14), (15), and (16) have been programmed for use on a digital computer. The integration of equations (11), (12), and (13) starts at  $s = 0$  and terminates at  $s = s^*$ ; the initial shockwave standoff distance  $\delta(0)$  is unknown and must be chosen so that equation (16) is satisfied at the correct corner location. A discussion of the techniques used in solving the equations and a detailed program list-out are given in reference 16

with sample calculations on certain blunt axisymmetric bodies. In order to use the existing program for more general shapes, it is necessary only to modify the input statements and the subroutine called BSR. In order to perform the calculations, an input statement was added to direct the computer to read in tabulated values of surface slope and  $r$  for any particular configuration. The subroutine BSR was modified by adding appropriate statements to direct the computer to use the correct values of surface slope and  $r$  for the particular configuration under consideration. With these modifications, flow conditions may be computed for any bluff body for which the surface slope is continuous and is given as a function of  $r$ .

### C. Calculation Procedure

In order to begin the iterative procedure involving equations (9) and (10) and equations (11) through (16), either a shape or a pressure distribution must be assumed. For the work contained herein, an initial shape was calculated using a Newtonian pressure distribution (i.e.,  $P = C_p = 2 \sin^2\theta$ ), and this shape was used in the integral relation computer program involving equations (11) through (16) to obtain a new pressure distribution. To satisfy the requirements of the integral relation computer program that the surface slopes be continuous and normal to the stream direction at the nose, the initial shape was given a spherical nose radius. The pressure distribution so obtained was fed into the linear membrane program involving equations (9) and (10) which calculated a new shape having a zero nose radius of curvature. The new shape was then spherically blunted and applied to repeat the

procedure until convergence occurred, and a unique shape and pressure were obtained. The process was considered to have converged if the difference between successive iterations resulted in a maximum variation in  $x/r_0$  of less than 0.0001.

## VIII. EXPERIMENT

### A. Models

Two pressure distribution models were wind tunnel tested as part of this investigation. The shapes and pertinent model dimensions are given in figure 4; model coordinates and orifice locations are given in table I. The model shapes were derived using the linear membrane equilibrium equations for values of  $Z = 0.65$  and  $\alpha = 0$ . For one of the shapes, a Newtonian pressure distribution was assumed, and for the other shape a pressure distribution predicted by integral relation theory was used. Both shapes had a nose-radius-to-base-radius ratio ( $r_n/r_b$ ) of 0.20. Each model was instrumented with 49 pressure orifices; 41 orifices were distributed along the front face of the model and 8 orifices were distributed along the model base. The orifices along the front face of the models were positioned along two radial lines  $180^\circ$  apart and were mounted flush with, and normal to, the model surface, whereas the base pressures were measured at the open ends of tubes soldered along the model base (see fig. 5). The models were machined from mild steel, and the surfaces were polished to a smooth bright finish.

### B. Test Apparatus

1. Test facility. - All tests were conducted in the Langley 9- by 6-foot thermal structures tunnel. This facility is a supersonic blow-down wind tunnel which operates at a Mach number of 3.0 at stagnation pressures from 50 to 200 psia and at stagnation temperatures from ambient to  $2,000^\circ$  F. The air storage capacity is sufficient to permit tests of

2 minutes' duration for stagnation pressures of 50 psia. The models were sting mounted as shown in figure 6. The models were aligned at zero angle of attack with respect to the tunnel walls.

2. Instrumentation. - Surface pressures were measured on each of the configurations by means of pressure transducers located outside the tunnel. The transducers were connected to the orifices by approximately 25 feet of 0.090-inch-inside-diameter steel tubing. In addition to the surface pressure orifices, four total pressure and four total temperature probes were mounted on the walls of the tunnel to monitor the free-stream flow conditions. Transducers with accuracies of  $\pm 1$  percent of the maximum range were used for all pressure measurements. Care was exercised in choosing transducers having a maximum range that matched the pressures to be measured as closely as possible. The outputs from all the pressure transducers and the thermocouples were recorded by the Langley central data recording facility.

### C. Test Procedure

All tests were conducted at a stagnation temperature of  $250^{\circ}$  F and at a stagnation pressure of 60 psia. The corresponding Reynolds number, based on the maximum body diameter, was approximately  $10.4 \times 10^6$ . Constant flow conditions were maintained for approximately 40 seconds in order to be certain that all pressures had stabilized. Both model shapes were tested twice at identical flow conditions in order to check for incorrect pressure readings and to determine the experimental accuracies involved. For the repeat test, the pressure transducers were interchanged.



## IX. THEORETICAL RESULTS AND DISCUSSION

### A. Comparison of Newtonian and Integral Relation

#### Pressure Distributions and Corresponding

#### Tension Shell Shapes

Tension shell shape coordinates that were computed using Newtonian pressure distributions and the corresponding coordinates that were obtained from the iteration procedure using integral relation theory described previously are presented in table II. For the present work, three Newtonian-derived tension shell shapes were used as initial shapes in the iteration procedure and were computed for values of the shape parameter,  $Z$ , of 0.50, 0.65, and 0.80. As the shape parameter is increased, the body length increases. Consequently, these values of  $Z$  were chosen to yield shapes that were sufficiently bluff to generate a detached bow shock wave and thus permitted use of the integral relation theory. For these shapes, a nose radius of  $r_n = 0.05 r_b$  was used in the integral relation computer program to obtain the pressure distributions used in the linear membrane computer program for determining shapes. Also included in table II are the shape coordinates that resulted from the studies made to observe effects of nose radius and Mach number on tension shell shapes derived from integral relation theory. In both of these studies, the shape for  $Z = 0.65$  was used. For the study on nose radius effects, shapes were computed for nose radii of  $r_n = 0.20 r_b$  and  $0.56 r_b$  and for  $M_\infty = 3.0$ . For the study on Mach number effects, shapes with  $r_n = 0.05 r_b$  were computed for Mach numbers of 2.50, 5.00, and 7.00. Corresponding pressure

distributions and drag coefficients predicted by the integral relation theory are listed in table III for all of the shapes given in table II.

The disparity between pressure distributions given by different theories for the same shape is illustrated in figure 7. Presented are the pressure distributions calculated from Newtonian, modified Newtonian, and integral relation theories for the Newtonian-derived tension shell shape for  $Z = 0.65$  and  $r_n = 0.05 r_b$ . The results are typical for all shapes considered herein and indicate considerable difference in predicted trends. For example, pressures obtained from the integral relation theory decrease from the stagnation point and are substantially higher over most of the surface with respect to the Newtonian and modified Newtonian values, whereas the Newtonian and modified Newtonian pressures increase from the nose cap tension shell juncture. The modified Newtonian pressures are presented in order to compare theoretical pressures based on the same free-stream Mach number; Newtonian theory is based on  $M_\infty = \infty$ . Except for the stagnation point values, the pressures obtained from modified Newtonian theory ( $C_p = C_{p,stag} \sin^2\theta$ ) are in no better agreement with the pressures given by integral relations theory than are the Newtonian pressures ( $C_p = 2 \sin^2\theta$ ).

The initial Newtonian-derived tension shell shape, the final iterated shape, and the pressure distributions used in their derivation are shown in figure 8 for  $Z = 0.50, 0.65$ , and  $0.80$ . The final iterated shapes shown were obtained after four iterations. This rapid convergence is demonstrated in figure 8(b) for the  $Z = 0.65$  shape. Typically, a substantial decrease in the overall length of the shape occurred with the first iteration. Second, third, and fourth iterations resulted in

consecutively smaller changes in overall length as shown by the detail in figure 8(b). Each successive iteration resulted in a shape with an overall length that was alternately shorter or longer than the preceding shape and thus indicated convergence. The pressure distributions converged in a similar manner, but smaller differences were obtained between successive iterations. The integral relation pressure values produced by the first and fourth iterated shapes are almost identical and are only slightly larger than the integral relation pressures calculated for the original Newtonian shape.

The results of figure 8 show that the pressures obtained from integral relation theory decrease as the tension shell length is increased but the changes in pressure are small compared to the changes in shape. In contrast, the Newtonian pressures show a strong sensitivity to shape change.

B. Effects of Nose Radius and Mach Number on Shapes and  
Pressure Distributions Derived From  
Integral Relation Theory

Since the integral relation pressure distributions and the derived tension shell shapes are somewhat dependent on the assumed nose radius and the free-stream flow conditions, it is desirable to document the effects of these variables. Therefore, pressure distributions and tension shell shapes were computed for  $L = 0.65$  at a Mach number of 3.0 with  $r_n/r_b = 0.20$  and 0.56 and for Mach numbers of 2.50, 3.00, 5.00, and 7.00 with  $r_n/r_b = 0.05$ . The effects resulting from the nose

radius and Mach number variations are shown in figures 9 and 10, respectively. The largest effect of nose radius on the pressure distribution occurs over the spherical nose cap and is characterized by a slight bulge which covers an increasing percentage of the surface area as the nose radius is increased, but the overall effects are small and substantiate the conclusions presented in reference 17 for configurations with the sonic point located at the shoulder. Therefore, tension shell shapes that are computed from the integral relation pressure distributions are insensitive to nose radius and a spherical nose cap may be added without appreciably affecting the shape downstream of the nose cap juncture. In contrast to these results, figure 10 shows that Mach number affects both the pressure distribution and the tension shell shape. An increase in Mach number results in a reduced static pressure loading and a shorter tension shell shape, but both the pressure distribution and the tension shell shape converge as the Mach number increases. The Mach number dependency and the fact that aerodynamic decelerators will be used over a finite Mach number range indicate that a tension shell shape derived for a specific application will be a compromised shape taking into account Mach number effects. Although a Mach number dependency is shown for the tension shell shape, the changes in shape that occur within the Mach number range considered herein are not as great as those obtained between Newtonian-derived and integral-relation-derived tension shell shapes.

## X. EXPERIMENTAL RESULTS AND DISCUSSION

A summary of the experimental pressures obtained from the Mach 3.0 wind-tunnel tests is provided in table IV in pressure-coefficient form and is presented graphically in figure 11 for the  $Z = 0.65$  Newtonian- and integral-relation-derived tension shell shapes with  $r_n/r_b = 0.20$ . The data from both models show excellent repeatability and indicate nearly identical pressure distributions in spite of the difference in the shapes. (See fig. 4.) Thus, the experimental results substantiate the conclusion, noted earlier from the computed integral relation pressure distributions of figure 8, that the pressure distribution for a bluff tension shell shape is relatively insensitive to significant changes in the tension shell shapes. For these shapes relatively high and nearly constant pressures are generated along the front surface to a value of  $r/r_b \approx 0.75$  before showing the influence of the flow expansion around the sharp corner at the base. Nearly constant values of pressure less than free-stream static pressure are obtained along the rear surface.

## XI. COMPARISON OF THEORY AND EXPERIMENT

### A. Pressure Distribution

In figure 11, curves of the pressures obtained from integral relation, Newtonian, and modified Newtonian theories are included, and it is apparent that the experimental data favor the curves given by integral relation theory. The agreement between experiment and integral relation theory is excellent over the nose cap and is within 9 percent over the remaining portion of the Newtonian-derived shape (fig. 11(a)) and within 7 percent for the iterated shape (fig. 11(b)). The experimentally determined pressures lie above the integral relation curve downstream of the nose-cap juncture, and the maximum deviation from theory occurs at a value of  $r/r_0 \approx 0.90$ . The deviation of integral relation theory from experiment may be due partially to viscous effects which were not taken into account by integral relation theory. These viscous effects result in a buildup of the boundary-layer displacement thickness along the model surface and therefore change the effective shape. However, integral relation theory gives a much better representation of the aerodynamic loading on bluff tension shell shapes than do the Newtonian theories and is recommended for use in design applications.

### B. Shapes Determined From Experimental Pressures

The experimental pressure distributions of figure 11 were used in the linear membrane computer program to determine shapes for comparison with the theoretically determined shapes. The coordinates of the experimental shapes and their corresponding experimental pressure

distribution in terms of the nondimensional membrane pressure differential,  $P$ , are given in table V. The pressures are an average of those obtained from the two tests conducted on each wind-tunnel model. These experimental shapes and their pressure distributions are compared with corresponding Newtonian-derived and integral-relation-derived shapes and pressure distributions in figure 12. In this figure, unlike figure 11, the experimental pressure values are generally less than obtained from integral relation theory because the experimental values of the parameter,  $P$ , were evaluated using measured values of base pressure, whereas the values of  $P$  determined from integral relation theory were evaluated assuming zero base pressure. The agreement between the experimental and integral relation values of  $P$ , however, is within 4 percent. The tension shell shapes derived from the experimental pressures differ by less than 2 percent and should be representative of shapes obtained under true aerodynamic loading. Moreover, these shapes are in excellent agreement with the integral-relation-derived shape. Consequently, a truer representation of a bluff tension shell shape can be obtained from pressures determined from integral relation theory rather than from Newtonian theory.

### C. Drag Coefficients

One criterion governing the final selection of a planetary atmosphere-entry decelerator shape is the drag coefficient. Therefore, the method used in estimating the drag coefficient is of paramount importance. In table VI, the drag coefficients predicted by Newtonian- and integral-relation theories for the  $Z = 0.65$  tension shell shapes

with  $r_n/r_b = 0.20$  are compared with drag coefficients obtained by integrating the experimental pressure distributions of figure 11. All drag coefficients are based on a free-stream static base pressure in order to provide a common basis for comparison. The drag coefficients predicted by Newtonian theory are up to 13 percent greater than experiment, whereas the drag coefficients predicted by integral relation theory are 6 percent less than experiment. Thus, conservative and more accurate estimates are obtained from integral relation theory.



## XII. CONCLUDING REMARKS

A theoretical and an experimental investigation were conducted for the purpose of improving accuracy in calculating pressure distributions for various tension shell decelerator shapes and to evaluate the effects on derived shapes resulting from the application of different pressure distributions. Although tension shell shapes have been derived using Newtonian aerodynamics in conjunction with linear membrane theory, experimental pressure distributions obtained on other bluff shapes indicated that Newtonian theory does not describe the actual pressure distribution. However, better agreement has been obtained for many bluff shapes with sonic corners by means of integral relation theory. Consequently, a computational procedure involving the use of a one-strip integral relation technique for calculating pressure distributions was devised for use in deriving new tension shell shapes. The results indicated that tension shell shapes that are derived using pressure distributions predicted by integral relation theory are substantially blunter than equivalent Newtonian tension shell configurations. Although the pressure distributions predicted by integral relation theory are somewhat dependent on model nose radius and Mach number, the differences in the integral-relation-derived tension shell shapes attributable to various nose radii and Mach numbers are considerably less than those noted between Newtonian- and integral-relation-derived tension shell shapes.

Experimental pressure distributions were obtained at a Mach number of 3.0 in the Langley 9- by 6-foot thermal structures tunnel for typical

Newtonian- and integral-relation-derived tension shell shapes. The experimental pressure distributions were in relatively good agreement with theoretical pressure distributions predicted by integral relation theory but showed poor agreement with pressure distributions predicted by Newtonian and modified Newtonian theories. Tension shell shapes derived using the experimental pressure distributions were in good agreement with the corresponding integral-relation-derived tension shell shape but were in poor agreement with Newtonian tension shell shapes. Thus, integral-relation-derived tension shell shapes are more representative of bluff tension shell shapes than Newtonian-derived shapes. Drag coefficients predicted by integral relation theory were approximately 6 percent less than experimental values whereas Newtonian drag coefficients were up to 13 percent higher than experiment.

### XIII. REFERENCES

1. Anderson, M. S., Robinson, J. C., Bush, H. G., and Fralich, R. W.:  
A Tension Shell Structure For Application to Entry Vehicles.  
NASA TN D-2675, 1965.
2. Deveikis, W. D., and Sawyer, J. W.: Aerodynamic Characteristics of  
Tension Shell Shapes at Mach 3.0. NASA TN D-3633, 1966.
3. Robinson, J. C., and Jordan, A. W.: Exploratory Experimental  
Aerodynamic Investigation of Tension Shell Shapes at Mach  
7.0. NASA TN D-2994, 1965.
4. Bernot, P. T.: Longitudinal Stability Characteristics of Several  
Proposed Planetary Entry Vehicles at Mach 6.73. NASA TN D-2785,  
1965.
5. Creel, T. R.: Longitudinal Aerodynamic Characteristics of a  
Tension Shell Entry Configuration at Mach 20.0. NASA  
TN D-3541, 1966.
6. Anderson, R. A.: Structures Technology - 1964. Astronautics and  
Aeronautics, Vol. 2, No. 12, December 1964, pp. 14-20.
7. Roberts, L.: Entry Into Planetary Atmospheres. Astronautics and  
Aeronautics. Vol. 2, No. 10, October 1964, pp. 22-29.
8. Sawyer, J. W., and Deveikis, W. D.: Effects of Configuration  
Modifications on Aerodynamic Characteristics of Tension  
Shell Shapes at Mach 3.0. NASA TN D-4080, 1967.
9. Harris, Charles P.: Transonic Aerodynamic Investigation of Tension  
Shell and Blunted  $100^\circ$  Conical Shapes For Unmanned Entry Vehicles.  
NASA TN D-3700, 1966.

10. Sawyer, J. W.: Comparison of the Mach 3.0 Aerodynamic Characteristics of Tension String, Tension Shell, and  $120^\circ$  Conical Shapes. NASA TN D-4360, 1968.
11. Turk, R. A.: Pressure Measurements on Rigid Model of Ballute Decelerator at Mach Numbers From 0.56 to 1.96. NASA TN D-3545, 1966.
12. Penland, J. A., and Bernot, P. T.: Aerodynamic Characteristics of Three Axisymmetric Low-Fineness-Ratio Re-entry Shapes at Mach 6.9. NASA TN D-4122, 1967.
13. Campbell, J. F., and Howell, D. T.: Supersonic Aerodynamics of Large-Angle Cones. NASA TN D-4719, 1968.
14. Deveikis, W. D., and Sawyer, J. W.: Effects of Cone Angle, Base Flare Angle, and Corner Radius on Mach 3.0 Aerodynamic Characteristics of Large-Angle Cones. NASA TN D-5048, 1969.
15. Baker, D. C.: Investigation of an Inflatable Decelerator Attached to a  $120^\circ$  Conical Entry Capsule at Mach Numbers From 2.55 to 4.40. AEDC-TR-68-227, 1968.
16. South, J. C., Jr.: Calculation of Axisymmetric Supersonic Flow Past Blunt Bodies With Sonic Corners, Including a Program Description and Listing. NASA TN D-4563, 1968.
17. Ward, L. Christopher, and Pugh, Philip G.: Shock Standoff Distances of Blunt and Sharp Cones. AIAA Journal, Vol. 6, No. 10, October 1968, pp. 2018-2019.

#### XIV. VITA

The author was born in [REDACTED], on [REDACTED].  
He was graduated from the Moore County High School, Lynchburg, Tennessee, in 1959 and received a Bachelor of Science degree in Mechanical Engineering from Tennessee Technological University in 1964. Since graduation the author has been employed with the National Aeronautics and Space Administration at Langley Research Center as an Aero-Space Technologist.

*James Wayne Sawyer*

## XV. APPENDIX A

In this section the Fortran IV source program is listed for the derivation of tension shell structures of revolution subject to linear membrane theory and axisymmetric pressure distribution. The following definitions are used in the program and are defined below or in the list of symbols:

<u>Program</u>	<u>Definition</u>
Z	Z
ALPHA	$\alpha$
THETAD	Limiting configuration slope, deg
THE(J)	Radial position array, R
P(J)	Pressure distribution array, P
J	Indexing Parameter
K	Indexing Parameter
DR	Integration step size
THET	$\theta$ , deg
RO	R
YO	X

```

      PROGRAM SAWYER  (INPUT,OUTPUT,TAPE5=INPUT,TAPE6=OUTPUT,PUNCH)
C     PROGRAM FOR CALCULATION OF TENSION SHELL SHAPES
100  FORMAT(1X2HZ=E16.8,2X6HALPHA=E16.8,2X7HTHETAD=E16.8)
101  FORMAT(8X5HTHETA8X2HRO8X2HYO12X2HPO)
      1  FORMAT(3E16.8)
      2  FORMAT(2E16.8)
20   FORMAT(4E16.8)
      DIMENSION THE(500),P(500)
13   READ(5,1)Z,ALPHA,THETAD
      READ(5,2)(THE(J),P(J),J=1,500)
      DEG=57.295780
      THETAS=1.5707962
      THETAR=THETAD/DEG
      RAN=1.5707000
      J=1
      RO=THE(J)
      DRO=.005
      DR=DRO
25   THETA=THETAS
      DTHET=THETA
      R=RO
      YO=0.
      K=1
      WRITE(6,100)Z,ALPHA,THETAD
      WRITE(6,101)
      THET=THETA*DEG
      WRITE(6,20)THET,RO,YO,PO
      PUNCH 2,THETA,RO
      L=1
C     COMPARISON OF ANGLES
3    IF(R.LT.THE(J).AND.R.GT.THE(J+1))GO TO 4
      IF(R.EQ.THE(J))GO TO 5
      IF(R.EQ.THE(J+1))GO TO 6
      IF(R.LT.THE(J+1))GO TO 7
      IF(R.GT.THE(J))GO TO 8
C     INTERPOLATION FOR THETA AND PRESSURE
4    DOG=(R-THE(J))/(THE(J+1)-THE(J))
      PO=P(J)+(P(J+1)-P(J))*DOG
      GO TO 9
5    PO=P(J)
      GO TO 9
6    PO=P(J+1)

```

```

      GO TO 9
7  J=J+1
   GO TO 3
8  J=J-1
   GO TO 3
C  RUNG-KUTTA INTEGRATION
9  IF(R.LE.0)GO TO 23
   ER=R** (1.-ALPHA)
   IF(THETA.GT.RAN)A=0.
   IF(THETA.GT.RAN)C=2.*Z*ER*PO
   IF(THETA.GT.RAN)GO TO 14
   TAN=SIN(THETA)/COS(THETA)
   A=-DR*ALPHA/(R*TAN)
   C=2.*Z*ER*PO/SIN(THETA)
14 IF(K.EQ.2)GO TO 10
   IF(K.EQ.3)GO TO 11
   IF(K.EQ.4)GO TO 12
   A1=A-DR*C
   IF(THETA.GT.RAN)B1=0.
   IF(THETA.GT.RAN)GO TO 15
   B1=DR/TAN
15 R=R0-DR/2.
   THETA=DTHET+A1/2.
   K=K+1
   GO TO 3
10 A2=A-DR*C
   IF(THETA.GT.RAN)B2=0.
   IF(THETA.GT.RAN)GO TO 16
   B2=DR/TAN
16 K=K+1
   THETA=DTHET+A2/2.
   GO TO 3
11 A3=A-DR*C
   IF(THETA.GT.RAN)B3=0.
   IF(THETA.GT.RAN)GO TO 17
   B3=DR/TAN
17 K=K+1
   R=R0-DR
   THETA=DTHET+A3
   IF(R.LE.0)C=0
   IF(R.LE.0)GO TO 12
   GO TO 3
12 A4=A-DR*C

```



```

      IF(THETA.GT.RAN)B4=0.
      IF(THETA.GT.RAN)GO TO 18
      B4=DR/TAN
18  DELTA=1./6.*(A1+2.*A2+2.*A3+A4)
      DTHET=DTHET+DELTA
      THETA=DTHET
      THET=THETA*DEG
      RO=RO-DR
      DY=1./6.*(R1+2.*B2+2.*B3+B4)
      YO=YO+DY
C   PRINT RESULTS
      WRITE(6,20)THET,RO,YO,PO
      PUNCH 2,THETA,RO
      K=1
      IF(R.LE.0)GC TO 23
      IF(THETA.GT.THETAR)GO TO 3
23  CONTINUE
      STOP
      END

```

TABLE I. - COORDINATES AND ORIFICE LOCATIONS FOR NEWTONIAN- AND INTEGRAL-RELATION-DERIVED PRESSURE DISTRIBUTION MODELS.

ORIFICE NO.	NEWTONIAN SHAPE		INTEGRAL RELATION SHAPE		ORIFICE NO.	NEWTONIAN SHAPE		INTEGRAL RELATION SHAPE	
	$x/r_b$	$r/r_b$	$x/r_b$	$r/r_b$		$x/r_b$	$r/r_b$	$x/r_b$	$r/r_b$
1	0.4113	0	0.3588	0	26	0.0811	0.625	0.0630	0.625
2	0.4097	0.025	0.3572	0.025	27	0.0712	0.650	0.0549	0.650
3	0.4049	0.050	0.3525	0.050	28	0.0619	0.675	0.0474	0.675
4	0.3967	0.075	0.3442	0.075	29	0.0532	0.700	0.0404	0.700
5	0.3845	0.100	0.3320	0.100	30	0.0450	0.725	0.0339	0.725
6	0.3680	0.125	0.3167	0.125	31	0.0375	0.750	0.0279	0.750
7	0.3510	0.150	0.3010	0.150	32	0.0306	0.775	0.0226	0.775
8	0.3341	0.175	0.2854	0.175	33	0.0244	0.800	0.0178	0.800
9	0.3174	0.200	0.2701	0.200	34	0.0188	0.825	0.0135	0.825
10	0.3008	0.225	0.2550	0.225	35	0.0139	0.850	0.0099	0.850
11	0.2845	0.250	0.2401	0.250	36	0.0098	0.875	0.0068	0.875
12	0.2685	0.275	0.2256	0.275	37	0.0063	0.900	0.0043	0.900
13	0.2527	0.300	0.2114	0.300	38	0.0036	0.925	0.0024	0.925
14	0.2371	0.325	0.1975	0.325	39	0.0016	0.950	0.0010	0.950
15	0.2219	0.350	0.1839	0.350	40	0.0004	0.975	0.0002	0.975
16	0.2071	0.375	0.1707	0.375	41	0.0001	0.987	0.0001	0.987
17	0.1925	0.400	0.1579	0.400		0	1.000	0	1.000
18	0.1784	0.425	0.1456	0.425	42	*	0.987	*	0.987
19	0.1646	0.450	0.1336	0.450	43	*	0.900	*	0.900
20	0.1513	0.475	0.1221	0.475	44	*	0.800	*	0.800
21	0.1384	0.500	0.1111	0.500	45	*	0.700	*	0.700
22	0.1259	0.525	0.1005	0.525	46	*	0.600	*	0.600
23	0.1140	0.550	0.0904	0.550	47	*	0.500	*	0.500
24	0.1025	0.575	0.0808	0.575	48	*	0.400	*	0.400
25	0.0915	0.600	0.0716	0.600	49	*	0.300	*	0.300

\* Orifices installed on the base of the model

TABLE II. - COORDINATES FOR NEWTONIAN- AND INTEGRAL-RELATION-DERIVED TENSION SHELL SHAPES.

NEWTONIAN SHAPES				INTEGRAL RELATION SHAPES											
Z	0.50	0.65	0.80	0.50	0.65	0.65	0.65	0.65	0.65	0.65	0.65	0.65	0.65	0.65	0.80
M <sub>00</sub>	∞	∞	∞	3.00	2.50	3.00	5.00	7.00	3.00	3.00	3.00	3.00	3.00	3.00	3.00
γ	1.00	1.00	1.00	1.40	1.40	1.40	1.40	1.40	1.40	1.40	1.40	1.40	1.40	1.40	1.40
r <sub>n</sub> /r <sub>b</sub>	0	0	0	0.05	0.05	0.05	0.05	0.05	0.05	0.05	0.05	0.05	0.05	0.20	0.05
r/r <sub>b</sub>	x/r <sub>b</sub>	x/r <sub>b</sub>	x/r <sub>b</sub>	x/r <sub>b</sub>	x/r <sub>b</sub>	x/r <sub>b</sub>	x/r <sub>b</sub>	x/r <sub>b</sub>	x/r <sub>b</sub>	x/r <sub>b</sub>	x/r <sub>b</sub>	x/r <sub>b</sub>	x/r <sub>b</sub>	x/r <sub>b</sub>	x/r <sub>b</sub>
0	.3430	.4546	.5734	.2928	.4081	.3971	.3865	.3843	.3972	.3973	.3972	.3843	.3972	.3973	.5211
0.050	.3169	.4198	.5290	.2695	.3748	.3647	.3550	.3531	.3648	.3648	.3648	.3531	.3648	.3648	.4769
0.100	.2910	.3852	.4849	.2463	.3417	.3326	.3238	.3221	.3326	.3327	.3326	.3221	.3326	.3327	.4332
0.150	.2654	.3510	.4414	.2235	.3092	.3010	.2931	.2916	.3010	.3010	.3010	.2916	.3010	.3010	.3903
0.200	.2402	.3174	.3986	.2012	.2774	.2701	.2631	.2618	.2701	.2701	.2701	.2618	.2701	.2701	.3486
0.250	.2156	.2845	.3569	.1794	.2466	.2401	.2340	.2329	.2401	.2402	.2401	.2329	.2401	.2402	.3085
0.300	.1917	.2527	.3164	.1584	.2170	.2113	.2061	.2050	.2114	.2114	.2114	.2050	.2114	.2114	.2702
0.350	.1686	.2219	.2775	.1383	.1888	.1839	.1794	.1785	.1839	.1839	.1839	.1785	.1839	.1839	.2340
0.400	.1464	.1925	.2404	.1192	.1622	.1579	.1541	.1534	.1579	.1580	.1579	.1534	.1579	.1580	.2000
0.450	.1254	.1646	.2052	.1011	.1372	.1336	.1304	.1298	.1336	.1337	.1336	.1298	.1336	.1337	.1684
0.500	.1055	.1384	.1722	.0843	.1141	.1111	.1084	.1079	.1111	.1111	.1111	.1079	.1111	.1111	.1394
0.550	.0870	.1140	.1416	.0688	.0929	.0904	.0882	.0878	.0904	.0904	.0904	.0878	.0904	.0904	.1129
0.600	.0700	.0915	.1136	.0547	.0736	.0716	.0699	.0696	.0716	.0717	.0716	.0696	.0717	.0717	.0892
0.650	.0545	.0712	.0882	.0420	.0565	.0549	.0536	.0534	.0549	.0550	.0549	.0534	.0549	.0550	.0682
0.700	.0407	.0532	.0658	.0309	.0415	.0404	.0394	.0392	.0404	.0404	.0404	.0392	.0404	.0404	.0499
0.750	.0288	.0375	.0463	.0215	.0288	.0279	.0272	.0271	.0279	.0280	.0279	.0271	.0279	.0280	.0345
0.800	.0187	.0244	.0301	.0137	.0183	.0170	.0173	.0172	.0178	.0178	.0178	.0172	.0178	.0178	.0219
0.850	.0107	.0139	.0172	.0076	.0102	.0099	.0096	.0096	.0099	.0099	.0099	.0096	.0099	.0099	.0121
0.900	.0048	.0063	.0077	.0033	.0045	.0043	.0042	.0041	.0043	.0043	.0043	.0041	.0043	.0043	.0053
0.950	.0012	.0016	.0020	.0008	.0011	.0010	.0010	.0009	.0010	.0010	.0010	.0009	.0010	.0010	.0013
1.000	0	0	0	0	0	0	0	0	0	0	0	0	0	0	0

TABLE III. - INTEGRAL RELATION PRESSURE DISTRIBUTIONS AND DRAG COEFFICIENTS FOR TENSION SHELL SHAPES.

NEWTONIAN SHAPES				INTEGRAL RELATION SHAPES											
$z$	0.50	0.65	0.80	0.50	0.65	0.80	0.50	0.65	0.80	0.50	0.65	0.80	0.50	0.65	0.80
$M_{\infty}$	$\infty$	$\infty$	$\infty$	3.00	2.50	3.00	3.00	2.50	3.00	3.00	2.50	3.00	3.00	2.50	3.00
$\gamma$	1.00	1.00	1.00	1.40	1.40	1.40	1.40	1.40	1.40	1.40	1.40	1.40	1.40	1.40	1.40
$r_p/r_b$	0	0	0	0.05	0.05	0.05	0.05	0.05	0.05	0.05	0.05	0.05	0.05	0.05	0.05
$x/r_b$	$p/q_{\infty}$	$p/q_{\infty}$	$p/q_{\infty}$	$p/q_{\infty}$	$p/q_{\infty}$	$p/q_{\infty}$	$p/q_{\infty}$	$p/q_{\infty}$	$p/q_{\infty}$	$p/q_{\infty}$	$p/q_{\infty}$	$p/q_{\infty}$	$p/q_{\infty}$	$p/q_{\infty}$	$p/q_{\infty}$
0	1.9142	1.9142	1.9142	1.9142	1.9485	1.9142	1.9142	1.8657	1.8526	1.8657	1.8526	1.9143	1.9143	1.9143	1.9142
0.050	1.8895	1.8729	1.8309	1.8944	1.9110	1.8802	1.8802	1.8348	1.8218	1.8348	1.8218	1.9013	1.9013	1.9095	1.8480
0.100	1.8782	1.8531	1.7943	1.8848	1.8963	1.8651	1.8651	1.8184	1.8048	1.8184	1.8048	1.8639	1.8639	1.8984	1.8211
0.150	1.8659	1.8354	1.7798	1.8745	1.8816	1.8504	1.8504	1.8039	1.7905	1.8039	1.7905	1.8487	1.8487	1.8798	1.8034
0.200	1.8536	1.8203	1.7663	1.8640	1.8682	1.8373	1.8373	1.7917	1.7788	1.7917	1.7788	1.8368	1.8368	1.8552	1.7909
0.250	1.8405	1.8072	1.7564	1.8534	1.8560	1.8255	1.8255	1.7813	1.7690	1.7813	1.7690	1.8254	1.8254	1.8260	1.7917
0.300	1.8301	1.7956	1.7487	1.8429	1.8449	1.8148	1.8148	1.7721	1.7605	1.7721	1.7605	1.8148	1.8148	1.8077	1.7743
0.350	1.8188	1.7851	1.7423	1.8324	1.8344	1.8048	1.8048	1.7638	1.7528	1.7638	1.7528	1.8049	1.8049	1.8019	1.7681
0.400	1.8075	1.7752	1.7365	1.8218	1.8243	1.7953	1.7953	1.7558	1.7455	1.7558	1.7455	1.7953	1.7953	1.7940	1.7622
0.450	1.7961	1.7656	1.7308	1.8108	1.8143	1.7857	1.7857	1.7478	1.7374	1.7478	1.7374	1.7857	1.7857	1.7756	1.7562
0.500	1.7843	1.7557	1.7248	1.7993	1.8040	1.7757	1.7757	1.7394	1.7303	1.7394	1.7303	1.7758	1.7758	1.7756	1.7496
0.550	1.7717	1.7452	1.7178	1.7868	1.7930	1.7650	1.7650	1.7295	1.7215	1.7295	1.7215	1.7650	1.7650	1.7650	1.7418
0.600	1.7578	1.7335	1.7093	1.7728	1.7808	1.7528	1.7528	1.7191	1.7111	1.7191	1.7111	1.7529	1.7529	1.7516	1.7325
0.650	1.7419	1.7198	1.6987	1.7568	1.7668	1.7386	1.7386	1.7060	1.6986	1.7060	1.6986	1.7387	1.7387	1.7388	1.7208
0.700	1.7231	1.7032	1.6849	1.7378	1.7501	1.7214	1.7214	1.6897	1.6827	1.6897	1.6827	1.7215	1.7215	1.7216	1.7076
0.750	1.7000	1.6823	1.6666	1.7141	1.7294	1.6997	1.6997	1.6685	1.6620	1.6685	1.6620	1.6998	1.6998	1.7000	1.6864
0.800	1.6700	1.6548	1.6415	1.6836	1.7025	1.6711	1.6711	1.6399	1.6338	1.6399	1.6338	1.6713	1.6713	1.6715	1.6599
0.850	1.6289	1.6163	1.6056	1.6415	1.6657	1.6313	1.6313	1.5993	1.5935	1.5993	1.5935	1.6315	1.6315	1.6317	1.6222
0.900	1.5674	1.5578	1.5500	1.5785	1.6106	1.5709	1.5709	1.5367	1.5308	1.5367	1.5308	1.5712	1.5712	1.5714	1.5642
0.950	1.4592	1.4538	1.4496	1.4674	1.5127	1.4633	1.4633	1.4248	1.4185	1.4248	1.4185	1.4638	1.4638	1.4787	1.4597
1.000	1.0114	1.0114	1.0114	1.0114	1.0295	1.0114	1.0114	0.9857	0.9788	0.9857	0.9788	1.0114	1.0114	1.0114	1.0114
$C_D$	1.519	1.500	1.478	1.532	1.480	1.516	1.516	1.582	1.602	1.582	1.602	1.516	1.516	1.517	1.498

TABLE IV. - EXPERIMENTAL PRESSURE DATA FOR  $Z = 0.65$   
TENSION SHELL SHAPES WITH  $r_n/r_b = 0.20$ .

ORIFICE NO	C <sub>p</sub>				ORIFICE NO	C <sub>p</sub>			
	NEWTONIAN SHAPE		INTEGRAL RELATION SHAPE			NEWTONIAN SHAPE		INTEGRAL RELATION SHAPE	
	TEST 1	TEST 2	TEST 3	TEST 4		TEST 1	TEST 2	TEST 3	TEST 4
1	1.756	1.757	1.758	1.755	26	1.645			1.650
2	1.752			1.751	27	1.649	1.652	1.658	1.655
3	1.739	1.741	1.747	1.746	28	1.638	1.637	1.640	1.643
4	1.720	1.720	1.722	1.723	29	1.641	1.640	1.645	1.645
5	1.702	1.704	1.718	1.718	30	1.622	1.629	1.630	1.627
6	1.695	1.698	1.707	1.704	31		1.630	1.633	
7	1.694	1.695	1.708	1.708	32	1.617	1.617	1.616	1.618
8	1.686	1.687	1.698	1.697	33	1.613	1.613	1.611	1.610
9	1.694	1.687	1.700	1.699	34	1.592	1.593	1.591	1.588
10	1.679	1.680	1.691	1.690	35	1.581	1.587	1.581	1.575
11	1.679	1.679	1.693	1.692	36	1.559	1.553	1.549	1.554
12	1.674	1.674	1.685	1.685	37	1.539	1.537	1.528	1.528
13	1.674	1.674	1.689	1.690	38	1.492	1.493	1.484	1.484
14	1.670	1.671	1.680	1.679	39	1.446	1.451	1.432	1.426
15	1.671	1.670	1.686	1.686	40	1.325	1.323	1.311	1.314
16	1.667	1.664	1.676	1.679	41	1.202	1.204	1.194	1.192
17	1.666	1.671	1.683	1.682	42	-0.067	-0.062	-0.060	-0.072
18	1.660	1.660	1.673	1.672	43	-0.078	-0.076	-0.076	-0.078
19	1.662	1.662	1.679	1.678	44	-0.077	-0.079	-0.078	-0.078
20	1.657	1.658	1.667	1.668	45	-0.095	-0.081	-0.080	-0.096
21	1.664	1.662	1.675	1.677	46	-0.093	-0.073	-0.097	-0.087
22	1.654	1.653	1.662	1.663	47	-0.057	-0.090	-0.094	-0.072
23	1.657	1.662	1.673	1.667	48	-0.076	-0.062	-0.072	-0.089
24		1.649	1.656		49	-0.097	-0.063	-0.098	-0.089
25	1.655	1.652	1.661	1.664					

TABLE V. - EXPERIMENTAL PRESSURE DISTRIBUTIONS AND THE DERIVED  $Z = 0.65$  TENSION SHELL SHAPES.

* EXPERIMENTAL CONFIGURATION I			** EXPERIMENTAL CONFIGURATION II		
P	$r/r_b$	$x/r_b$	P	$r/r_b$	$x/r_b$
1.830	0	0.3958	1.838	0	0.4015
1.815	0.050	0.3638	1.824	0.050	0.3680
1.779	0.100	0.3320	1.798	0.100	0.3348
1.766	0.150	0.3007	1.786	0.150	0.3030
1.758	0.200	0.2702	1.778	0.200	0.2721
1.751	0.250	0.2405	1.772	0.250	0.2421
1.745	0.300	0.2119	1.768	0.300	0.2132
1.742	0.350	0.1846	1.763	0.350	0.1857
1.739	0.400	0.1588	1.760	0.400	0.1597
1.736	0.450	0.1345	1.756	0.450	0.1352
1.734	0.500	0.1120	1.752	0.500	0.1125
1.729	0.550	0.0912	1.748	0.550	0.0916
1.724	0.600	0.0724	1.744	0.600	0.0727
1.717	0.650	0.0556	1.734	0.650	0.0558
1.708	0.700	0.0409	1.723	0.700	0.0410
1.696	0.750	0.0283	1.710	0.750	0.0284
1.680	0.800	0.0180	1.689	0.800	0.0180
1.653	0.850	0.0100	1.658	0.850	0.0110
1.610	0.900	0.0043	1.610	0.900	0.0043
1.510	0.950	0.0010	1.514	0.950	0.0010
0.925	1.000	0	0.933	1.000	0

\* Pressure distribution measured on  $Z = 0.65$  Newtonian tension shell shape with  $r_n/r_b = 0.20$  in  $M_\infty = 3.0$  airstream.

\*\* Pressure distribution measured on  $Z = 0.65$  integral relation tension shell shape with  $r_n/r_b = 0.20$  in  $M_\infty = 3.0$  airstream.

**TABLE VI. - THEORETICAL AND EXPERIMENTAL DRAG COEFFICIENTS FOR  
THE  $Z = 0.65$  NEWTONIAN- AND INTEGRAL-RELATION-  
DERIVED TENSION SHELL SHAPES WITH  $r_a/r_b = 0.20$ .**

CALCULATION METHOD	DRAG COEFFICIENT	
	NEWTONIAN SHAPE	INTEGRAL RELATION SHAPE
NEWTONIAN THEORY	1.759	1.814
INTEGRAL RELATION THEORY	1.500	1.516
EXPERIMENTAL	1.590	1.590

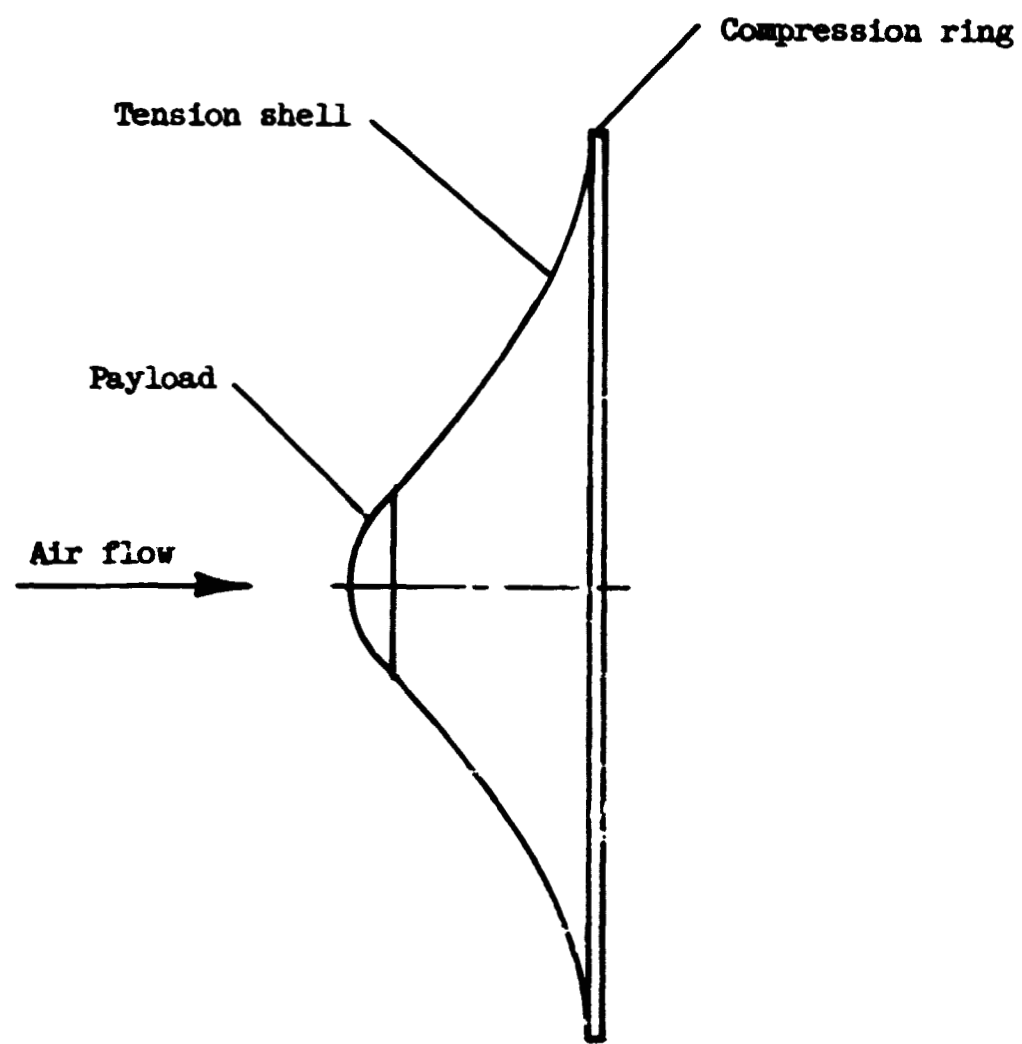


Figure 1.- Typical tension shell entry vehicle.



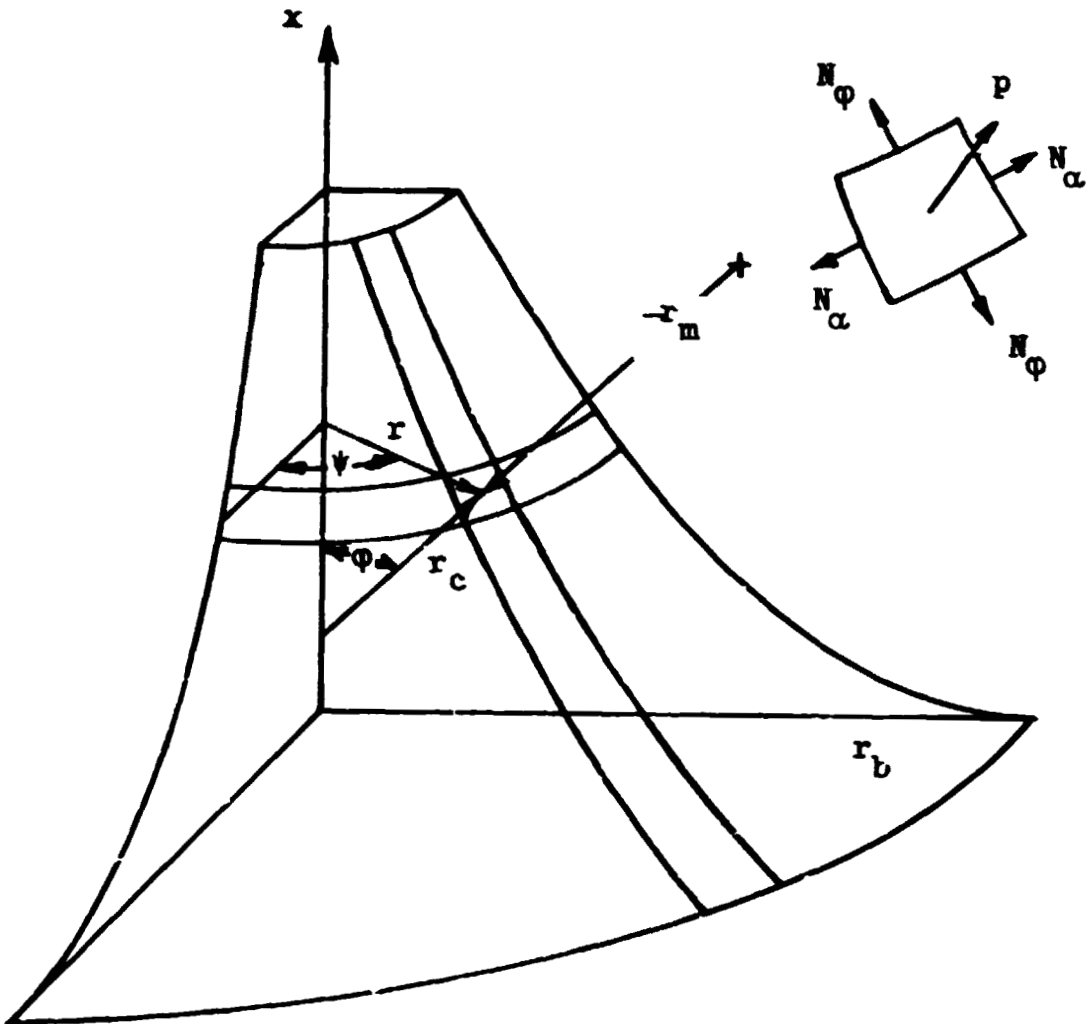


Figure 2.- Tension shell shape and coordinate system.

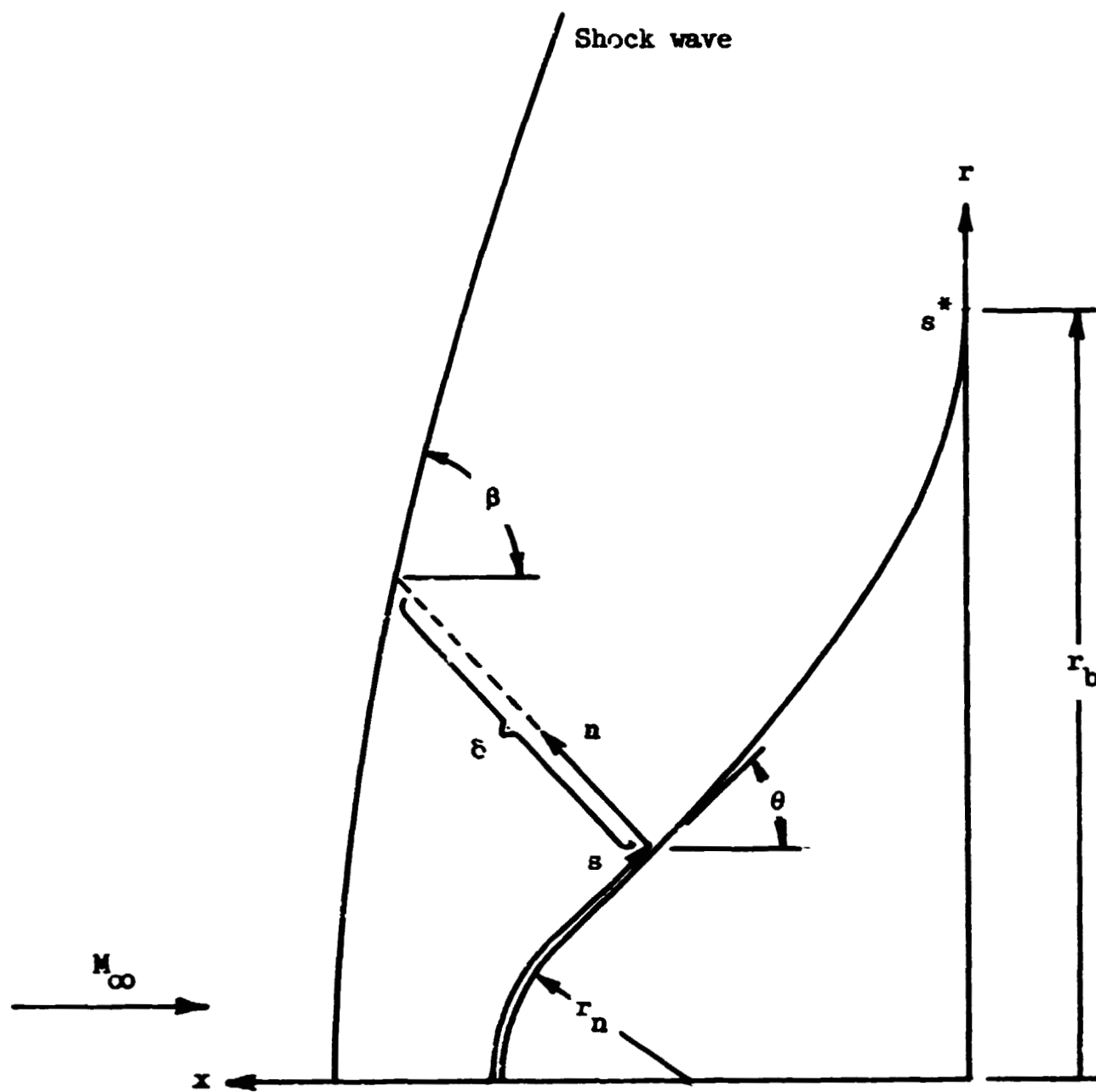


Figure 3.- Geometry and coordinate system for aerodynamic consideration.

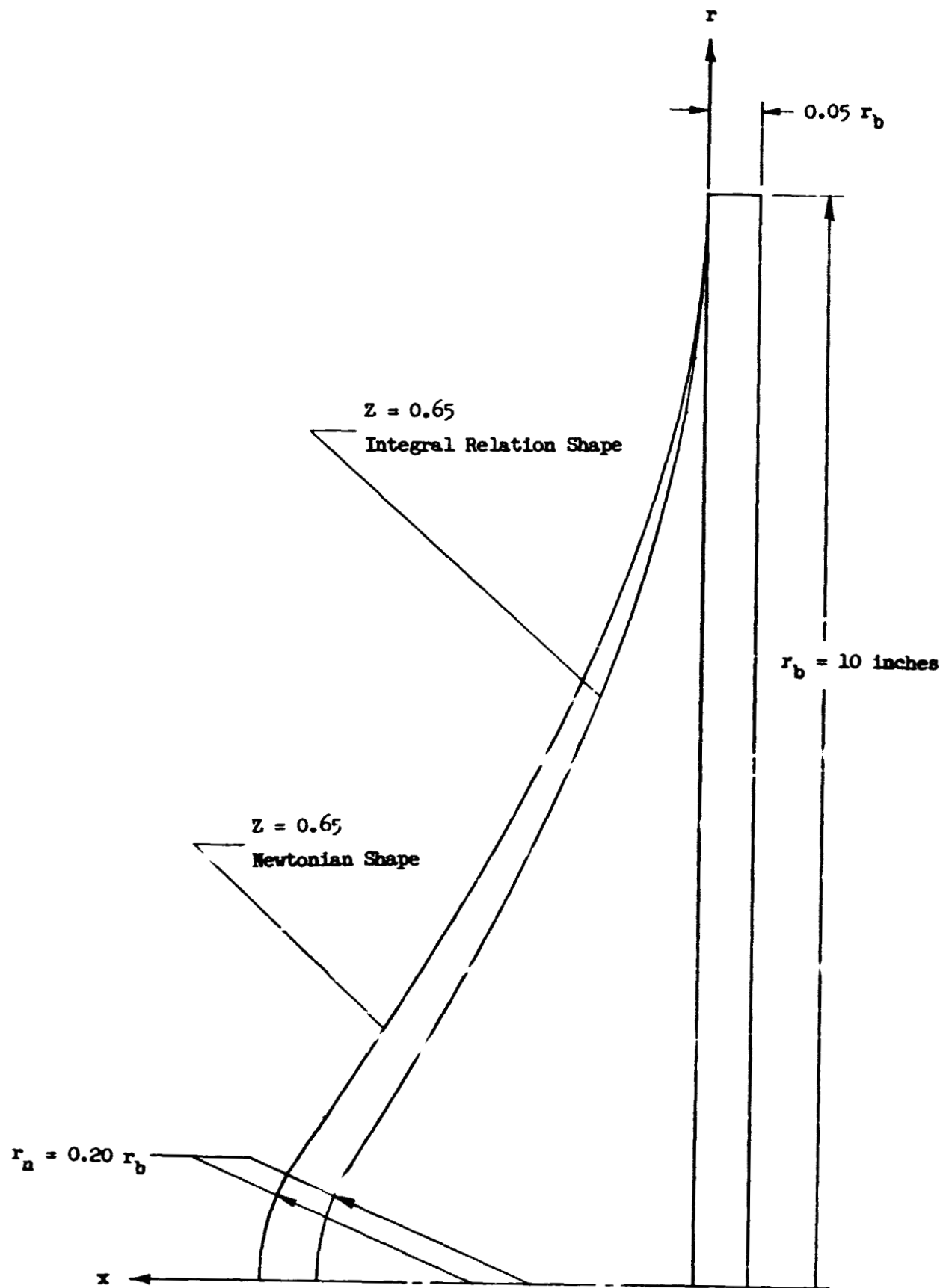


Figure 4.- Pressure distribution model details.

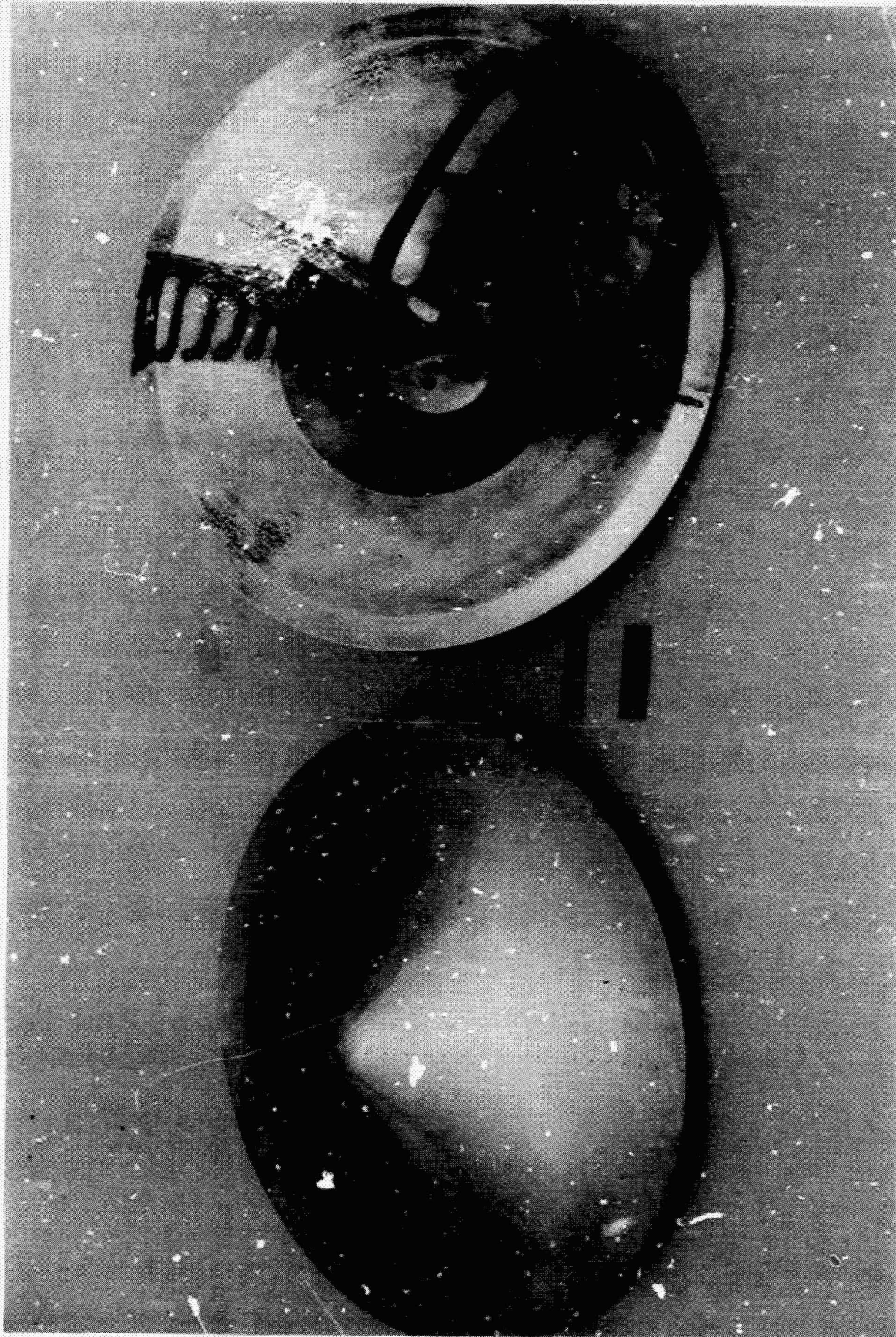


Figure 5.- Photograph of tension shell models.

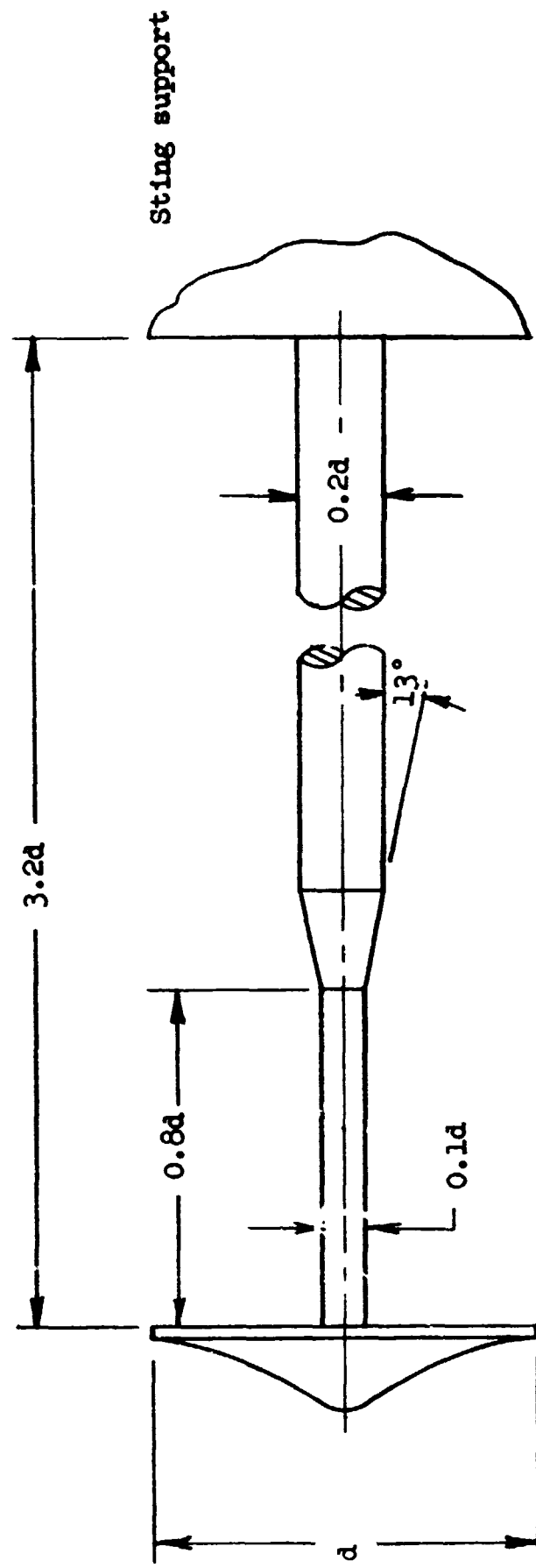


Figure 6.- Illustration of model sting mount system.

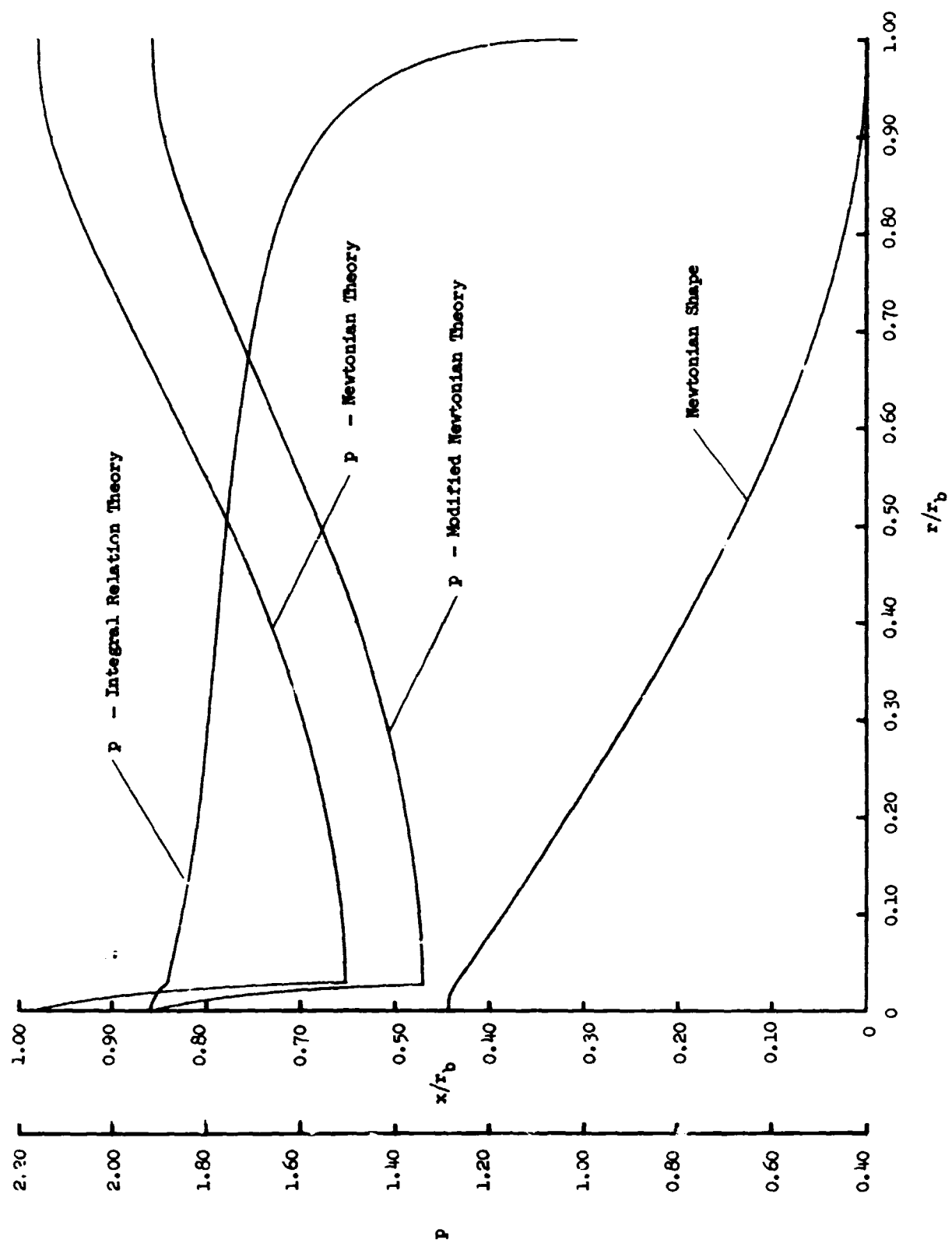
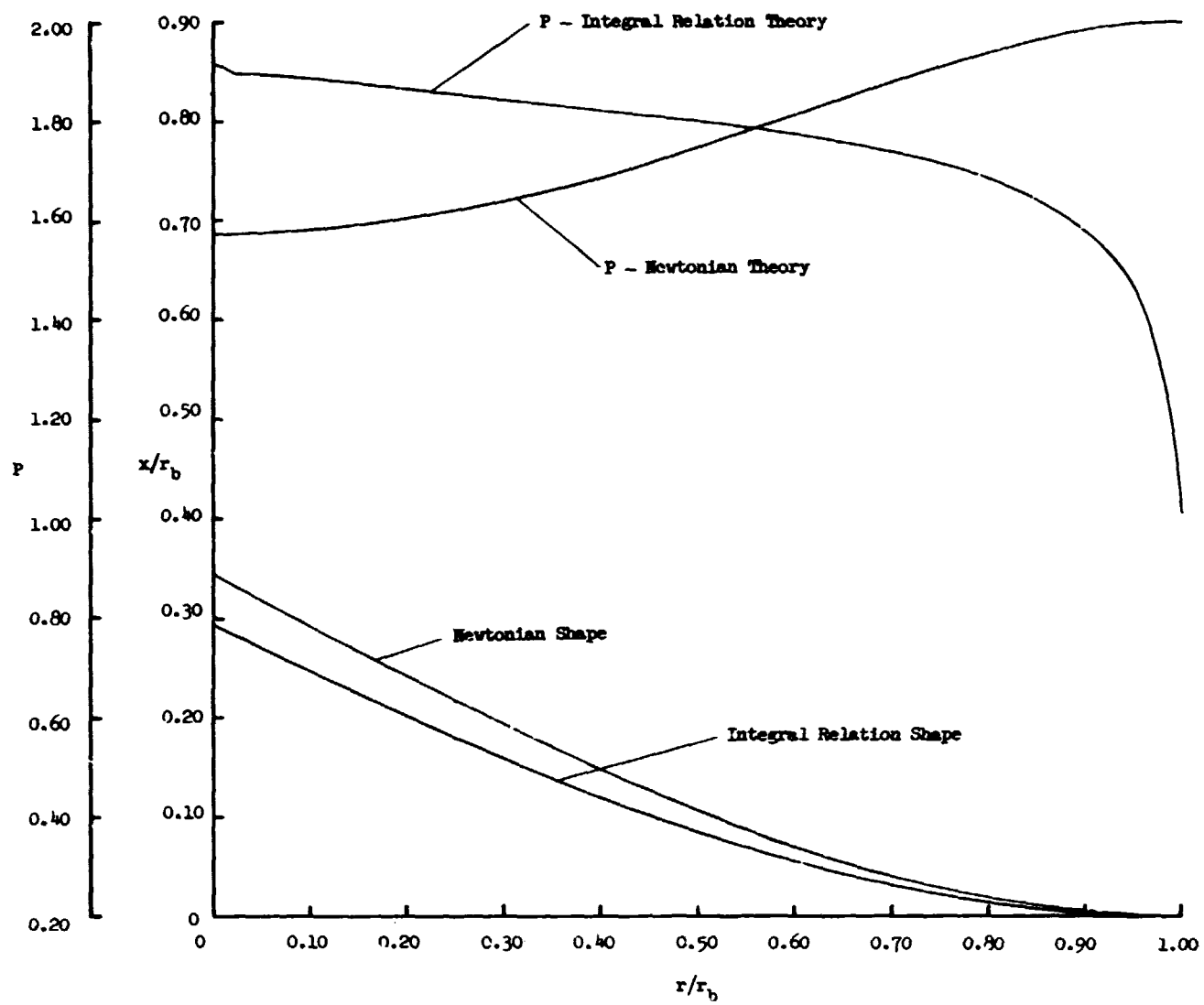
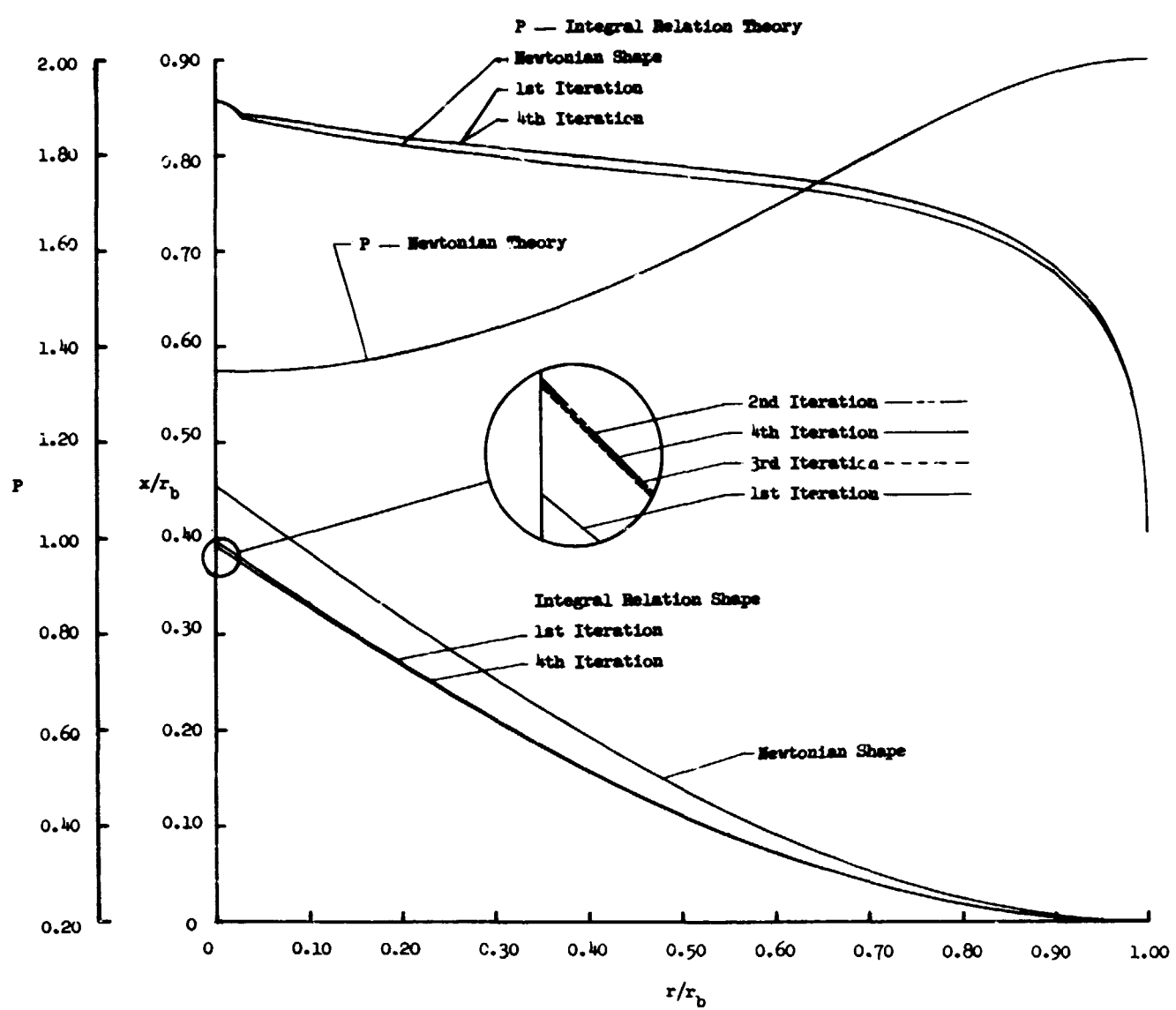


Figure 7.- Theoretical pressure distributions for the  $z = 0.65$  Newtonian-derived tension shell shape with  $r_n/r_b = 0.05$ .



(a)  $Z = 0.50$ .

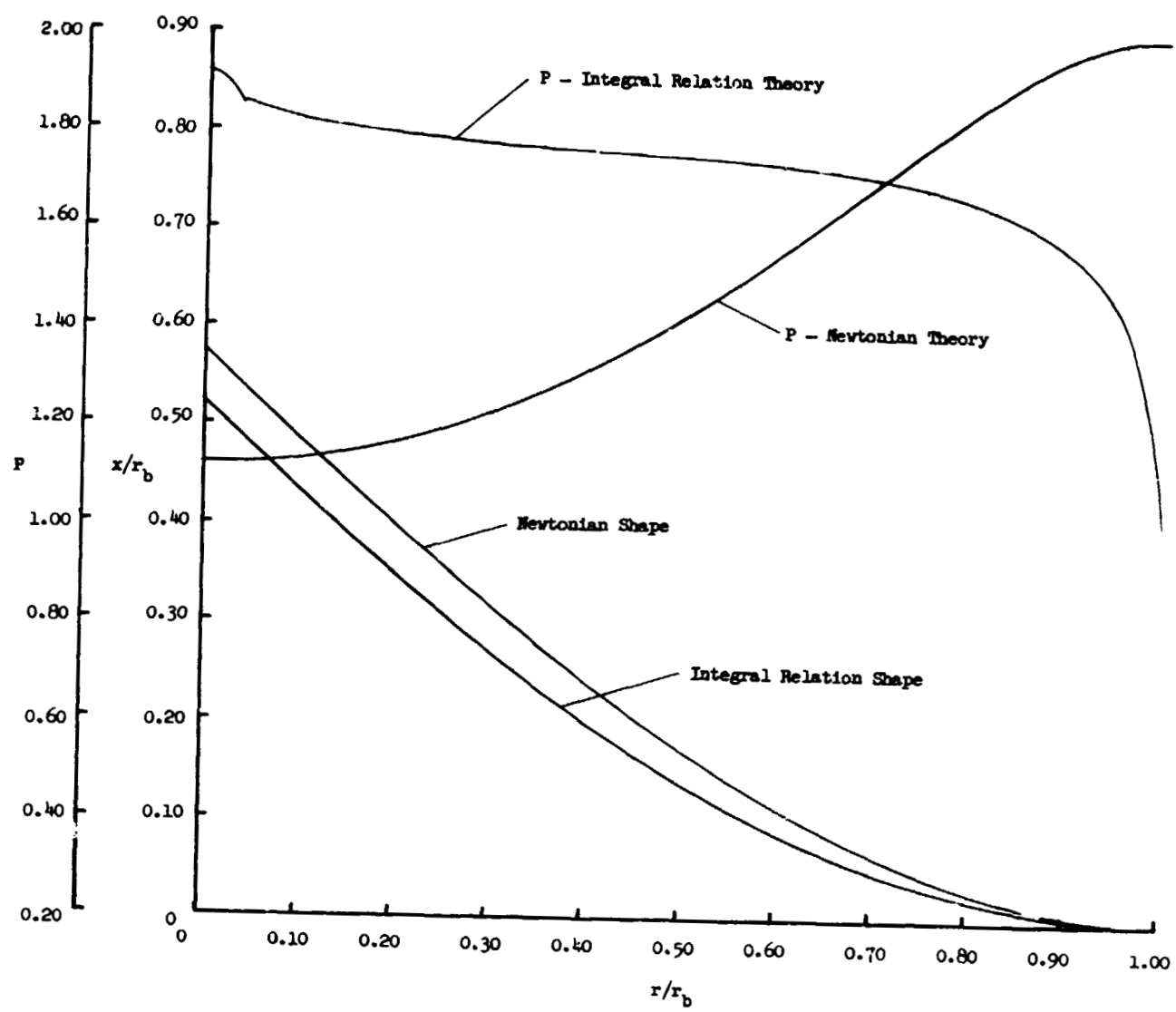
Figure 8.- Comparison of Newtonian and integral relation pressure distributions and corresponding tension shell shapes.



(b)  $Z = 0.65$ .

Figure 8.- Continued.





(c)  $Z = 0.80$ .

Figure 8.- Concluded.

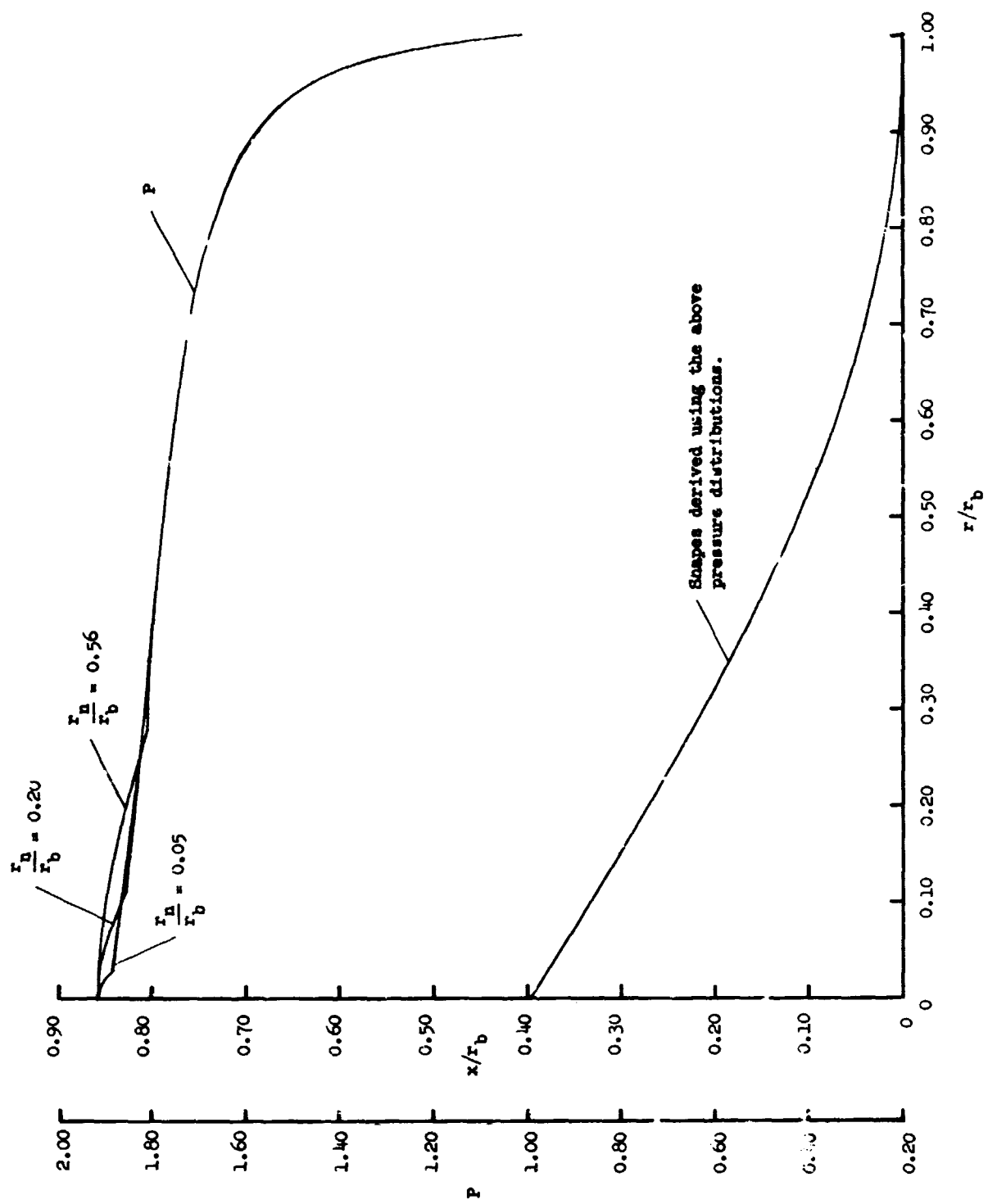


Figure 9.- Effects of nose radius on the integral relation pressure distributions and derived tension shell shapes at  $M_\infty = 3.0$ .

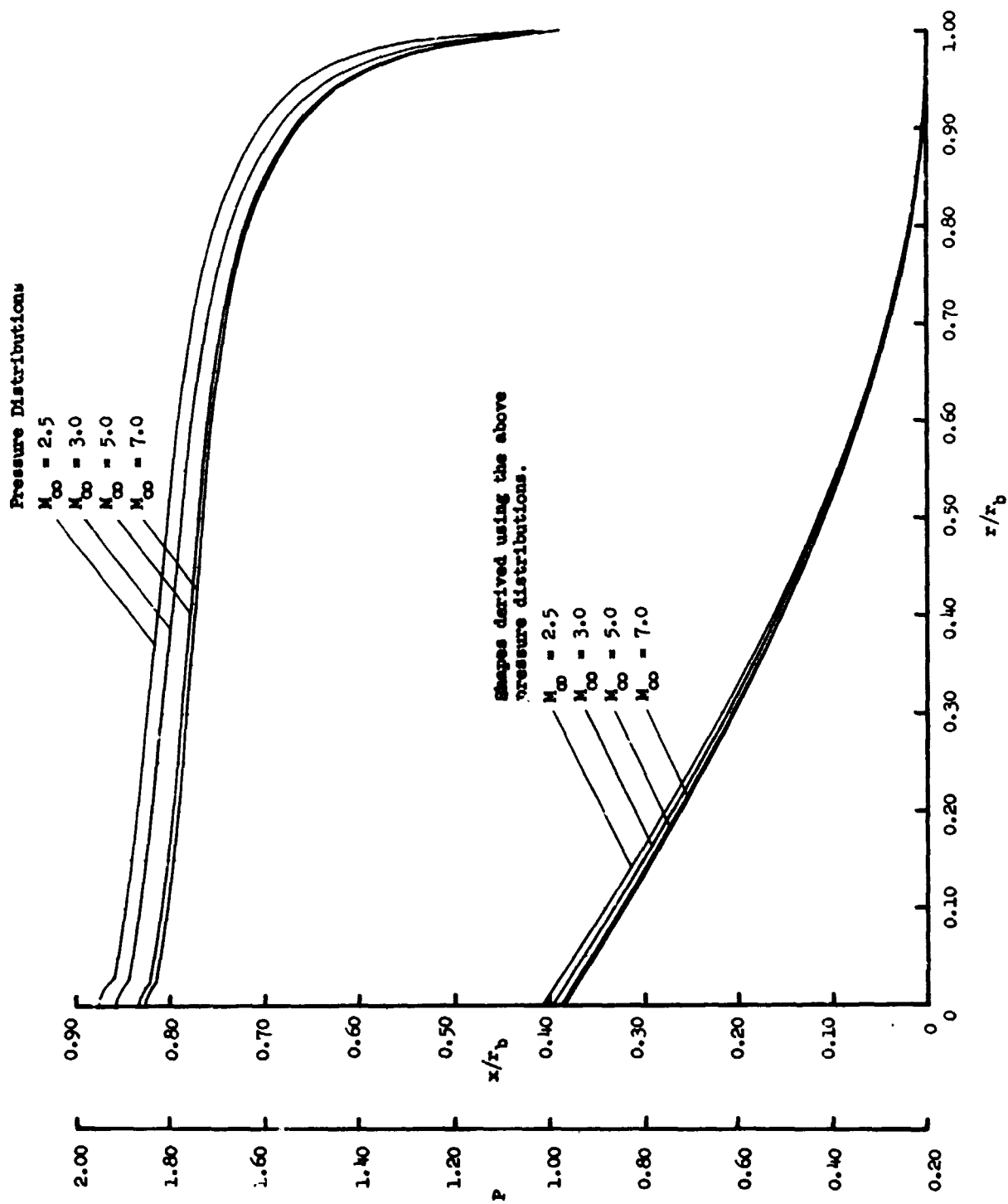
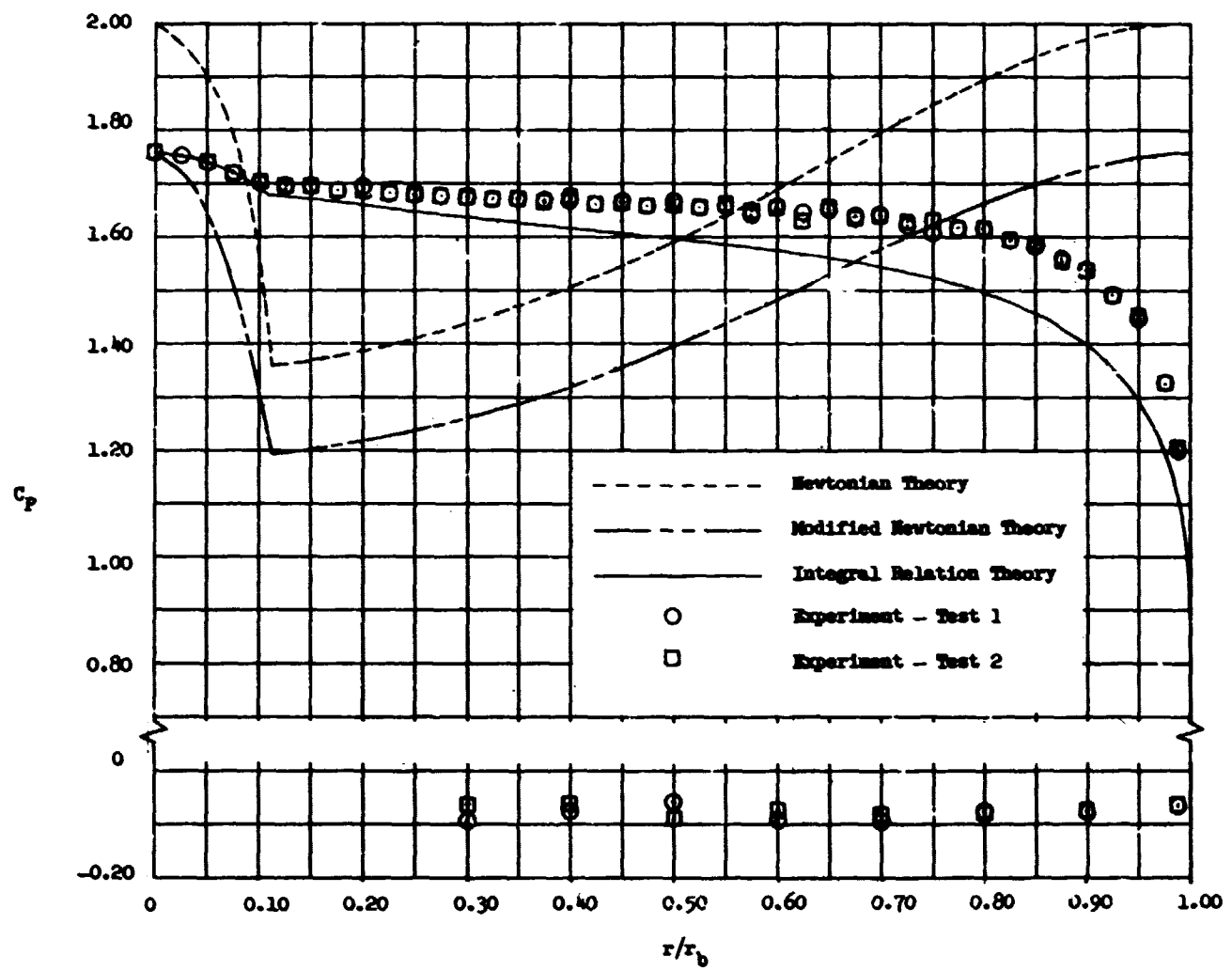
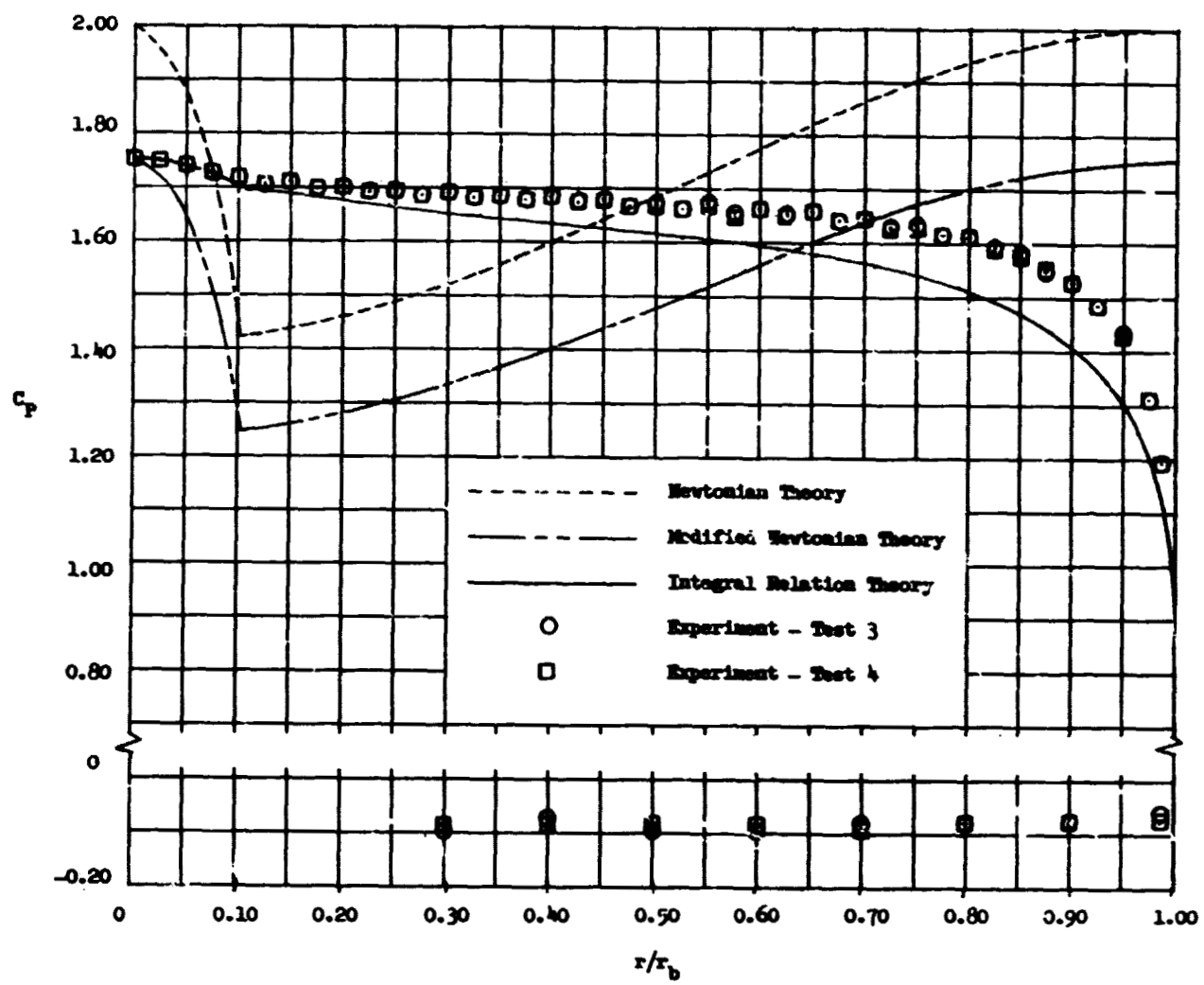


Figure 10.- Effects of Mach number on the integral relation pressure distributions and derived tension shell shapes with  $r_n/r_b = 0.05$ .



(a) Newtonian shape.

Figure 11.- Experimental and theoretical pressure distributions about the  $Z = 0.65$  Newtonian- and integral-relation-derived tension shell shapes with  $r_n/r_b = 0.20$  and at  $M_\infty = 3.0$ .



(b) Integral relation shape.

Figure 11.- Concluded.

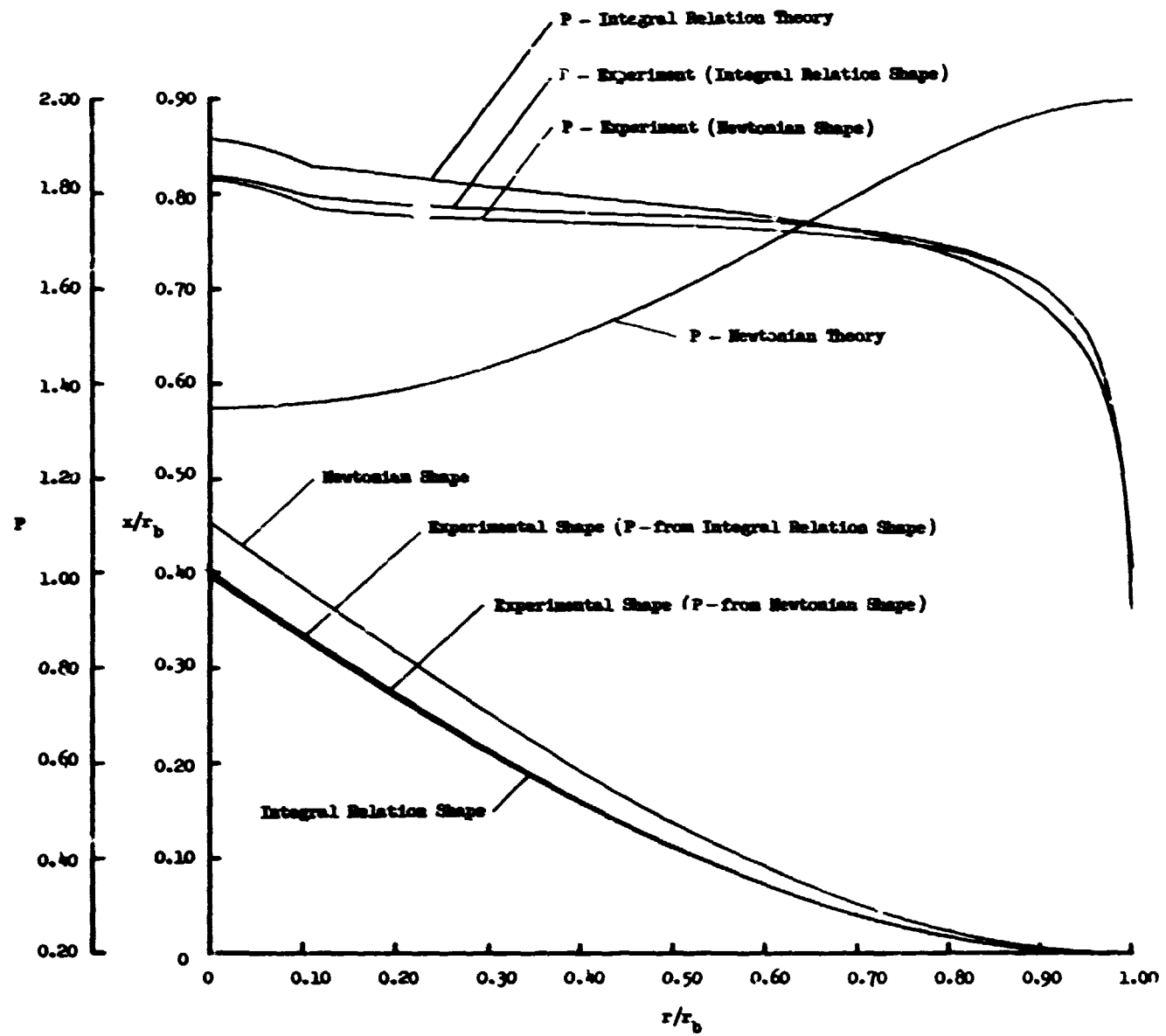


Figure 12.- Comparison of the  $Z = 0.65$  Newtonian-, integral-relation-, and experimentally derived tension shell shapes and pressure distributions.